# Four Stylized Facts about COVID-19*

Andrew G. Atkeson

*University of California, Los Angeles, NBER, and Federal Reserve Bank of Minneapolis*

Karen A. Kopecky

*Federal Reserve Bank of Atlanta and Emory University*

Tao Zha[1]

*Federal Reserve Bank of Atlanta, Emory University, and NBER*

Abstract. We develop a Bayesian method for estimating the dynamics of COVID-19 deaths and discover four key findings that expose the limitations of current structural epidemiological models. (1) Across 132 locations worldwide, daily death growth rates declined rapidly from high levels during the initial 30 days of the epidemic. (2) After this initial period, daily death growth rates fluctuated substantially around zero percent. (3) The cross-location standard deviation of death growth rates decreased rapidly in the first 10 days but remained high afterwards. (4) These insights apply to both effective reproduction numbers and their cross-location variability through epidemiological models.

*JEL Classification Nos:* C01, C02, C11, I1

*Keywords:* death growth rate, modified log-logistic function, noisy data, Bayesian estimation, structural break, SIR model, effective reproduction number, transmission rate

*Shortened Title:* **Four Stylized Facts about COVID-19**

*Manuscript received in April 2022; revised in March 2023.

[1]We are grateful to Jesus Fernandez-Villaverde (the editor) and three anonymous referees for their insightful comments, which have greatly improved this paper. Our gratitude also goes to Hongyi Fu for her exceptional research support, and to Ben Moll and James Stock for useful discussions. This paper combines our two earlier working papers: Atkeson et al. (2020a) and Atkeson et al. (2020b). The views expressed herein are those of the authors and do not necessarily reflect the views of the Federal Reserve Banks of Atlanta and Minneapolis, the Federal Reserve System, or the National Bureau of Economic Research.

# 1 Introduction

What are the key facts about the dynamic impacts on public health, in particular deaths, of the global COVID-19 pandemic? Structural epidemiological models with transmission rates that vary across time and locations are often used to understand the dynamics of a pandemic. From the perspective of these structural models, we are interested in not only cumulative total deaths, but also growth rates or first derivatives of cumulative deaths over time (daily deaths), and ideally, growth rates of growth rates or second derivatives of cumulative deaths over time (growth rates of daily deaths). These growth rates (second derivatives) are intimately connected to transmission rates of the deadly disease.

The reported daily deaths data regarding COVID-19 is considered to be the most reliable among all reported health data. The accuracy of the data during the early stages of the pandemic, however, was influenced by limitations in testing capacity and inaccuracies in reporting. The daily death data is also prone to noise caused by day-of-the-week effects and large spikes due to changes in the criteria used to classify COVID-19 deaths, as well as occasional reporting errors, which may result in negative daily death counts.

Given the noise in the data, we propose a probability density to model the *trend* of daily deaths, and an empirical specification that treats the noise and an approximation error as a random error around the trend. We present a Bayesian estimation procedure that is used to estimate our empirical specification of the trend in observed daily deaths from COVID-19 and the growth rate of that trend for many locations around the world over the course of the first year of the pandemic. We demonstrate the utility of this estimation procedure not only by applying it to the data on COVID-19 deaths for many locations around the world, but also by applying it to artificial data generated from a complex behavioral structural model of epidemiological dynamics. We then use this estimation procedure to establish four stylized facts about the dynamics of COVID-19 in the first year of the pandemic. And finally, we use a number of SIR epidemiological models, including more complex models similar to those considered by Fernandez-Villaverde and Jones (2020), to interpret these stylized facts

on COVID-19 deaths with the effective reproduction number and transmission rate of the disease.[2]

Our Bayesian estimation procedure is as follows. For each geographic location, we estimate an empirical specification for observed daily deaths from COVID-19 between an initial date $t_0$ at which cumulative deaths reached a threshold of 25 deaths and February 2, 2021 when the vaccine for COVID-19 became widely available.[3] The empirical specification is a mixture of modified log-logistic (MLL) density functions that is used to approximate the distribution of daily deaths over time.[4] The implications of our empirical specification for cumulative COVID-19 deaths are obtained by integrating these MLL density functions and those for the growth rate of daily deaths are obtained by differentiating them.

We work with MLL density functions because these density functions have bounded first derivatives. In particular, the derivative of the density in the left tail, corresponding to our estimate of the growth rate of daily deaths at the start of the pandemic, is controlled by a

[2]The *transmission rate* of the disease is defined as the average rate at which an infected individual contacts others and spreads the virus to those contacted. The *effective reproduction number* is defined as the average number of secondary cases infected by a single infected individual during his or her period of infectiousness when there are both susceptible and immune people among those contacted by this infected individual. Note that since a person who is no longer susceptible to the disease does not become infected even if he or she takes in the virus from contact with an infected individual, the effective reproduction number can vary due to changes in the transmission rate and changes in the portion of susceptible people among those contacted by infectious individuals.

[3]Our results do not change when the threshold is set to 50, 75, or 100. Epidemiologists are generally interested in the growth rate of daily deaths in the very early stage of an pandemic. We focus our empirical work on death data rather than case data. In this regard, we follow Murray (2020), Hay (2020), Korevaar et al. (2020), and Flaxman et al. (2020), who argue that data on COVID-19 related deaths is more accurate than testing data on cases. See also Aspelund et al. (2020) and https://www.cdc.gov/coronavirus/2019-ncov/cases-updates/about-serology-surveillance.html for a discussion of measurement errors in confirmed cases.

[4]Our specification bears a similarity to that used by Murray (2020) who uses a mixture of error functions to model cumulative COVID deaths. The purpose of this paper is not to compare our estimation procedure to other estimation techniques in the literature. Rather, the purpose is to document new stylized facts with our procedure and to use various SIR epidemiological models to interpret our empirical results.

parameter which we estimate. To evaluate the performance of our empirical specification in measuring the growth rate of daily deaths at the start of the pandemic, we conduct a Monte Carlo study in which we simulate artificial data from a complex behavioral structural model of disease dynamics covering a full year, add noise to that simulated data, and apply our estimation procedure to these artificial data. We find that our estimation procedure performs well, despite the fact that our empirical specification based on MLL density functions does not exactly correspond to the dynamics of daily deaths implied by the structural model. Based on this Monte Carlo experiment, we conclude that our estimation procedure is sufficiently flexible to capture the dynamics of COVID-19 both at the start and over the course of a full year of the pandemic.

We apply our estimation procedure to data on deaths from COVID-19 for 132 countries and states of the United States. Based on the estimation results from these locations, we present four "stylized facts" about the early dynamics of the COVID-19 pandemic. Note that in presenting these facts, we start our analysis of the dynamics of the pandemic in each location on the day that each location first reached 25 cumulative reported COVID-19 deaths. These four stylized facts are as follows:

(1) Within 30 days after the start of the pandemic, the growth rates of daily deaths fell rapidly from a wide range of initially high levels.
(2) After this initial period, growth rates of daily deaths fluctuated substantially around zero percent for the remainder of the first year of the pandemic.
(3) The cross-location dispersion of growth rates of deaths fell rapidly in the first 10 days of the pandemic but remained high subsequently.
(4) When interpreted through epidemiological models, these first three facts imply that both effective reproduction numbers and their cross-location dispersion fell rapidly within 30 days after the start of the pandemic.

In establishing our fourth stylized fact, we use several SIR epidemiological models, including more complex models similar to those considered by Fernandez-Villaverde and Jones (2020), to interpret the first three findings in terms of the effective reproduction number and transmission rate of the disease. In doing so, we invert the models with a time-varying

transmission rate to fit the estimated deaths data exactly.[5] In our baseline (the simplest) SIR model, the effective reproduction number is a linear transformation of the growth rate in logarithms of daily deaths, with the model-implied effective reproduction number equal to one when this growth rate is equal to zero and the slope of the relationship equal to the average number of days during which an infected individual is infectious to others. With our model inversion procedure, we are also able to recover an estimate of the evolution of the fraction of the population remaining susceptible over time.[6] With this fraction estimated, we show that the decline in the effective reproduction number (and its cross-location variation) is largely due to a decline in the transmission rate (and a decline in the cross-location variation in transmission rates). We then show that this fourth stylized fact holds for other more complex epidemiological models.

The first three stylized facts, taken together, demonstrate important differences in the evolutions of daily death growth rates early on versus later on in the COVID-19 pandemic. They indicate a structural break in the impact of COVID-19 on deaths occurring roughly 30 days after 25 cumulative deaths occurred.

Another important finding from our estimation is that the cross-location variation of death growth rates is much larger than the variation implied by model (parameter) uncertainty. Although our estimated parameters vary substantially, a majority of the dispersion of death growth rates at the beginning of the pandemic is attributable to cross-location variation. This finding is consistent with our Monte Carlo results in which our Bayesian procedure can uncover reasonably well the two divergent initial growth rates of deaths generated by the complex behavioral structural model, but the probability interval implied by the parameter uncertainty from our Bayesian procedure is much smaller than the distance between the two initial growth rates.[7]

[5]See also Atkeson (2020) and Atkeson et al. (2020a). Baqaee et al. (Forthcoming) use this procedure in their estimation of the effective reproduction number in the United States.

[6]We confirm our model estimates of this fraction by comparing them with findings from widespread serology studies for New York, Connecticut, Louisiana, and Spain.

[7]One should think of these divergent initial growth rates as those from two different locations.

The rest of this paper is organized as follows. Section II discusses the contribution of our paper to economic epidemiology. Section III presents MLL density functions for COVID-19 deaths. Section IV presents the Bayesian procedure for estimating our empirical specification for noisy data on COVID-19 deaths. Section V conducts a Monte Carlo study of how our mixture of MLL density functions can approximate very well the death paths from a very complex SIR model. Section VI presents the equations of a baseline SIR model and our procedure for inverting the SIR model for interpreting our empirical estimates of COVID-19 deaths. Section VII presents the key empirical findings from our Bayesian estimation of COVID-19 deaths. We conclude in Section IX.

## 2 Significance of our cross-location study

Our study, conducted across 132 locations worldwide, makes two important contributions to the literature on epidemiology, economics, and statistics. First, our results highlight the previously overlooked limitations of current structural models, including both epidemiological and economic models. Second, our Bayesian approach to estimating COVID-19 deaths represents a significant methodological advancement in statistical research.

### 2.1 Implications for epidemiological studies

Historical experience with prior respiratory epidemics, particularly influenza pandemics, did not lead epidemiologists to predict the dynamics of COVID-19 that we document. For example, Moore et al. (2020), which looked to pandemic influenza as a model for the future dynamics of COVID-19, emphasizes the importance of waves in characterizing the dynamics of past influenza pandemics, noting that of the eight major influenza pandemics since the early 1700's, "seven had an early peak that disappeared over the course of a few months without significant human intervention. Subsequently, each of those seven had a second substantial peak approximately six months after the first peak." While the patterns of daily deaths from COVID-19 did display peaks and valleys across locations, our finding that the growth rate of daily deaths over time and across locations fluctuated around zero percent after the initial month of the pandemic suggest that the dynamics of COVID-19 after the

initial wave were quite different from those in the first wave in that there were no longer periods of very rapid growth of the disease. In fact, in retrospect, it appears that the third scenario for the dynamics of COVID-19 offered in Moore et al. (2020), which they refer to as a "slow burn" of ongoing transmission, cases, and deaths not seen in prior influenza pandemics, came closest to the actual outcome for COVID-19.[8]

Further evidence on the discrepancies between the dynamics of COVID-19 that did occur and those projected by epidemiologists can be seen from mathematical modeling of pandemic influenza conducted prior to the outbreak of COVID-19. For example, as described in Germann et al. (2006) and Ferguson et al. (2006), an outbreak of pandemic influenza was anticipated to be short — on the order of three to four months in duration. In addition, epidemiological modelers expressed concern whether it would be even possible to reduce the effective reproduction number of a pandemic influenza below one based on social distancing in a Western democracy.[9] As discussed in Moore et al. (2020), this uncertainty regarding the efficacy of social distancing raised concerns about the possibilities for controlling the transmission of COVID-19 because COVID-19 has been more transmissible than observed in prior outbreaks of pandemic influenza. The early experience with the elimination of COVID-19 in China showed by late February of 2020 that control of this new disease through social distancing was possible, but it was unclear whether this outcome would be specific to a country with an authoritarian government and not reproducible elsewhere.

Our results reveal that a rapid decline in the effective reproduction number for COVID-19, from initially high values to fluctuations around one, was universally observed across locations worldwide. However, our measurement does not provide insights into whether this decline was due to social distancing measures or other mechanisms. Our study is similar to the work of Chowell et al. (2016), who aim to lay out stylized facts about early growth

[8]See also Kissler et al. (2020) for a long-term projection of the transmission dynamics of COVID-19 based on the observed dynamics of endemic coronaviruses.

[9]See, for example, Halloran et al. (2008), Hollingsworth et al. (2011), and Anderson et al. (2020). See Bootsma and Ferguson (2007) and Correia et al. (2022) for estimates of the impact of public health interventions on the dynamics of the 1918 Influenza Pandemic in U.S. cities.

patterns of various epidemics to guide subsequent modeling. To prepare for the next pandemic and draw lessons on how to contain the transmission of a new respiratory pathogen at lower economic and social cost, further research is needed to understand the mechanisms responsible for the initial decline in COVID-19's effective reproduction number and the factors that sustained the fluctuations of growth rates in daily deaths around zero percent for an extended period.

## 2.2 Implications for economics

Our findings also have implications for economists working on epidemics. Many economists have emphasized the role of human behavior in the form of voluntary social distancing in shaping the dynamics of COVID-19. In particular, many have argued that endogenous social distancing should be expected to keep the effective reproduction number of an epidemic near one as an equilibrium outcome.[10] The contrast between the dynamics of COVID-19 and prior influenza pandemics in the data raises questions for economists on how to reconcile models with these divergent disease dynamics.[11]

In addition, our quantitative findings regarding the extent of the variation in the growth rate of daily deaths from COVID-19 around zero percent in the data after the initial wave also present a challenge for economic modelers. Simple epidemiological models incorporating behavior, when calibrated to match the observed initial decline in the effective reproduction number of COVID-19, do not match the outcomes observed after the summer of 2020 without allowing for substantial changes in model parameters.[12] This is because such models imply

[10]For expositions and analyses of this hypothesis, see among others Bodenstein et al. (Forthcoming), Atkeson et al. (2021), Droste and Stock (2021), Keppo et al. (2021) (https://www.lonessmith.com/wp-content/uploads/2021/11/BSIR-final.pdf), John Cochrane's discussion at https://johnhcochrane.blogspot.com/2020/05/an-sir-model-with-behavior.html, Farboodi et al. (2020), Eichenbaum et al. (2020), Guerrieri et al. (2020), Gans (2020), Kaplan et al. (2020), Toxvaerd (2020), Eksin et al. (2019), and Phillipson and Posner (1993).

[11]Epidemiologists working on pandemic influenza were well aware of the potential importance of endogenous human responses to disease prevalence in impacting those dynamics. See, for example, Ferguson (2007) and Eksin et al. (2019).

[12]See, for example, Atkeson et al. (2021) and Figure 3 in Droste and Stock (2021).

such a strong response of behavior to current infections and/or deaths that the level of daily deaths implied by the model hardly fluctuates over time absent substantial shocks or changes in model parameters. The need for time variation in model parameters to match the data with simple epidemiological models incorporating behavior is likely the result of model misspecification. Much research needs to be done to find specifications of structural models of the impact of behavior on epidemiological dynamics that can account for the diversity in outcomes across locations and over time in a quantitatively plausible manner (see also Funk et al. (2015) for a discussion by epidemiologists of the challenges involved).

## 2.3 New estimation procedure

Our study represents a significant and novel contribution to the Bayesian methodology for estimating death growth rates caused by COVID-19. Our estimation method falls within the general Bayesian framework proposed by Shively et al. (2009) and Bornkamp and Ickstadt (2009). Unlike existing Bayesian methods that rely on cumulative monotone functions, however, our parametric approach leverages daily death data that has been overlooked in previous literature. By capturing the daily variation in the number of deaths caused by COVID-19, our method provides a more accurate and nuanced understanding of the rapid progression of the disease and the subsequent fluctuation of its growth rate.

More importantly, our approach not only ensures that the death growth rate (the second derivative of cumulative deaths) remains bounded but also enables us to account for multiple waves of deaths resulting from virus variants or other socio-economic factors. In Section VIII, we compare and contrast our method with alternative estimation techniques, highlighting their limitations and demonstrating the advantage of our approach in estimating the growth rate of COVID-19 deaths over both short and long time horizons. Accurate estimates of death growth rates are essential for monitoring and responding to the pandemic effectively and therefore are the necessary step to further scientific research on the implications of death dynamics for public health policy and decision-making.

## 3 Density functions for COVID-19 deaths

The data sources for daily deaths are New York Times for various states in the United States and Johns Hopkins University for other countries. To estimate the trend growth of daily deaths from these noisy data, we assume that the trend path of daily deaths in each location is given by a mixture of MLL density functions. In an early draft of our paper (Atkeson et al., 2020a), the Weibull probability density is used to model the trend path of daily deaths. As shown later in this section, the growth rate of the Weibull density is unbounded when the probability density approaches zero, which is an undesirable property of the Weibull density for our estimation purposes.

We model the distribution of deaths as

$$D(t) = D(\infty)F(t),$$

for $t \geq 0$ and zero otherwise, where $F(t)$ is a cumulative density function (CDF) and has a density almost everywhere. Here $D(\infty)$ is an unknown long run number of deaths with $F(0) = 0$ (and thus $D(0) = 0$). Denote the density function for $F(t)$ by $f(t)$. SIR models used in the literature imply that the derivative of the log of the density (the growth rate of deaths)

$$g(t) = \frac{f'(t)}{f(t)} \in \left[\underline{g}, \bar{g}\right]$$

should remain bounded by the finite values $\underline{g}$ and $\bar{g}$ for all $t \geq 0$. To keep the estimation feasible, we model $F(t)$ as a mixture of distributions $F_j(t)$ such that

$$F(t) = \sum_{j=1}^{J} w_j F_j(t),$$

where each $F_j$ satisfies the properties described above and $F_j(t) = 0$ for $t < 0$.

We consider two generalized families of distributions widely used in the literature. One is a generalized exponential distribution family and the other is a generalized logistic distribution family. For the generalized exponential family,

$$F_j(t) = 1 - \exp(-H_j(t)),$$

for $t \geq 0$, where $H_j(0) = 0$, $H_j(t) \to \infty$ as $t \to \infty$, and $H_j(t)$ is differentiable and strictly increasing. The first condition ensures that $F_j(0) = 0$, the second and the requirement that $H_j$ be increasing imply that $F_j$ is a CDF, and the differentiability requirement gives us the following density function:

$$f_j(t) = \exp(-H_j(t))H_j'(t).$$

Hence,

$$\log f_j(t) = -H_j(t) + \log H_j'(t)$$

and

$$g(t) = \frac{d \log f_j(t)}{dt} = \frac{f_j'(t)}{f_j(t)} = -H_j'(t) + \frac{H_j''(t)}{H_j'(t)}. \tag{1}$$

In Atkeson et al. (2020a) (an early draft of our paper), we use the Weibull distribution with

$$H_j(t) = \left(\frac{t}{a_j}\right)^{b_j}.$$

It follows from equation (1) that the growth rate of the Weibull density is unbounded as $t \to 0$ or as the density with $b_j > 1$ approaches zero. Unboundedness is an undesirable property of the Weibull density because boundedness is required by any distribution of deaths produced by an SIR model with bounded transmission rates.

To address this undesirable property, we consider a generalized logistic distribution family with

$$F_j(t) = \frac{H_j(t)}{1 + H_j(t)}$$

for $t \geq 0$ and zero otherwise. This distribution has density

$$f_j(t) = \frac{H_j'(t)(1 + H_j(t)) - H_j'(t)H_j(t)}{(1 + H_j(t))^2} = \frac{H_j'(t)}{(1 + H_j(t))^2}, \tag{2}$$

and

$$\log f_j(t) = \log H_j'(t) - 2 \log (1 + H_j(t)).$$

Hence,

$$g_j(t) = \frac{d \log f_j(t)}{dt} = \frac{f_j'(t)}{f_j(t)} = \frac{H_j''(t)}{H_j'(t)} - 2\frac{H_j'(t)}{(1 + H_j(t))}. \tag{3}$$

If

$$H_j(t) = \left(\frac{t}{a_j}\right)^{b_j},$$

$F_j(t)$ is a log-logistic CDF. From equation (3) one can show that growth rates of the log-logistic density are bounded as the density approaches zero, but unbounded as $t \to 0$. To have bounded growth rates as $t \to 0$, we modify the log-logistic distribution with

$$H_j(t) = \left(\frac{t+q}{a_j}\right)^{b_j} - \left(\frac{q_j}{a_j}\right)^{b_j},$$

for $q > 0$. It follows from equation (3) that the MLL density function is

$$g_j(t) = \frac{b_j - 1}{t + q_j} - 2\frac{\frac{b_j}{a_j}\left(\frac{t+q_j}{a_j}\right)^{b_j-1}}{1 + \left(\frac{t+q_j}{a_j}\right)^{b_j} - \left(\frac{q_j}{a_j}\right)^{b_j}}.$$

We can see from this expression that $g_j(t)$ remains bounded as $t \to 0$. The key parameter $q_j$ controls the relationship between the level of daily deaths and the growth rate of daily deaths on the left side of the support of the MLL distribution.

## 4 Estimation methodology and results

We model observed daily deaths as the sum of a mixture of MLL density functions and a residual whose magnitude is regime-specific. The regime-switching residuals allow us to effectively deal with erratic noise in the data. The Bayesian procedure allows us to construct posterior probability bands around the estimates. It also allows us to derive smooth estimates of the first and higher derivatives of daily deaths except for a finite number of points when one density function transitions to another one. The smoothness is needed to recover estimates of the effective reproduction numbers and transmission rates of the disease from various SIR models studied in the literature.

## 4.1 The likelihood function

Our estimation methodology begins by normalizing the cumulative death data in location $i$ so that $D_i(t)/(1+d_i)D_i(T)$ lies between zero and one, where $D_i(T)$ is the cumulative number of deaths in location $i$ at the end of the estimation period. The parameter $d_i > 0$ does not affect the model dynamics except scaling the cumulative deaths $D_i(t)$ so that $(1+d_i)D_i(T)$ approximates $D_i(\infty)$. We estimate $d_i$ together with other parameters in the model. Let $\Delta D_{i,t}^{\text{Data}}$ be the daily measured object for $dD_i(t)/dt$ and denote

$$\Delta \widetilde{D}_{i,t}^{\text{Data}} = \frac{\Delta D_{i,t}^{\text{Data}}}{D_{i,T}^{\text{Data}}},$$

$$\Delta \widetilde{D}_{i}^{t,\,\text{Data}} \equiv \left\{ \Delta \widetilde{D}_{i,t}^{\text{Data}},\, \Delta \widetilde{D}_{i,t-1}^{\text{Data}},\, \Delta \widetilde{D}_{i,t-2}^{\text{Data}},\, \ldots\, \Delta \widetilde{D}_{i,\,t_{i,0}}^{\text{Data}} \right\},$$

$$\Delta \widetilde{D}_{i}^{\text{Data}} \equiv \left\{ \Delta \widetilde{D}_{i,\,t_{0,i}}^{\text{Data}},\, \cdots,\, \widetilde{D}_{i,T}^{\text{Data}} \right\},$$

where $t_{0,i}$ is the time when the cumulative death toll reached 25 in location $i$.

Given the *noisy* daily death data, we run a non-linear regression with a mixture of MLL density functions and regime-switching heteroskedastic errors:

$$\Delta \widetilde{D}_{i,t}^{\text{Data}} = (1+d_i) \sum_{j=1}^{\mathcal{J}} w_{i,j}\, f_{i,j}\left(t - t_{0,i} - c_{i,j}\right) + \sigma_{i,k_t} \varepsilon_{i,t}, \tag{4}$$

where $\varepsilon_{i,t}$ is an iid standard normal random residual, weights $w_{i,j}$ are non-negative and sum to one across $j$, and $f_{i,j}$ is defined as in equation (2) with an additional subscript indexed by location $i$ and the corresponding parameters $a_{i,j}, b_{i,j}, q_{i,j}$ when $t - t_{0,i} - c_{i,j} \geq 0$. The density $f_{i,j}$ is equal to zero when $t - t_{0,i} - c_{i,j} < 0$. It follows from equation (2), with the additional subscript for location $i$, that for $t - t_{0,i} - c_{i,j} \geq 0$,

$$f_{i,j}\left(t - t_{0,i} - c_{i,j}\right) = \frac{\frac{b_{i,j}}{a_{i,j}} \left( \frac{t - t_{0,i} - c_{i,j} + q_{i,j}}{a_{i,j}} \right)^{b_{i,j}-1}}{\left[ 1 + \left( \frac{t - t_{0,i} - c_{i,j} + q_{i,j}}{a_{i,j}} \right)^{b_{i,j}} - \left( \frac{q_{i,j}}{a_{i,j}} \right)^{b_{i,j}} \right]^2}. \tag{5}$$

The parameters $c_{i,j}$ can be negative, positive, or zero; they help control the date at which each density in the mixture starts relative to the date $t_{0,i}$ when cumulative deaths first reach

25 in location $i$.[13] For the regime-switching volatility parameter $\sigma_{i,k_t}$, the switching state $k_t \in \{1, \ldots, \mathcal{K}\}$ follows a Markov-switching process and can accommodate both a large surge in daily deaths and a low death volatility typically associated with a low number of deaths. The transition matrix $\mathcal{Q}^k$ for $k_t$ is unrestricted except that each column of $\mathcal{Q}^k$ sums to one. Given the model parameters, we calculate the estimates of growth rates of daily deaths as

$$g_i(t) = \Delta \log \sum_{j=1}^{\mathcal{J}} w_{i,j}\, f_{i,j}\left(t - t_{0,i} - c_{i,j}\right). \tag{6}$$

Let $\theta_i$ represent a collection of 1) $a_{i,j}$, $b_{i,j}$, $q_{i,j}$, $c_{i,j}$, $d_i$, and $w_{i,j}$ for $j = 1, \ldots, \mathcal{J}$, 2) $\sigma_{i,1}, \cdots, \sigma_{i,\mathcal{K}}$, and 3) all the free parameters in the transition matrix $\mathcal{Q}^k$. From equation (4) one can derive the (log) conditional likelihood function for $\Delta \widetilde{D}_i^{t,\,\text{Data}}$ as

$$\begin{aligned}
&\log \mathcal{L}\left(\Delta \widetilde{D}_{i,t}^{\text{Data}} \mid \Delta \widetilde{D}_i^{t-1,\,\text{Data}}, k_t, \theta_i\right) = \\
&\qquad \log \mathcal{L}\left(\Delta \widetilde{D}_{i,t}^{\text{Data}} \mid k_t, \theta_i\right) = -\frac{T - t_{0,i}}{2}\log(2\pi) - \sum_{t=t_{0,i}}^{T} \log(\sigma_{i,k_t}) \\
&\qquad\qquad - \sum_{t=t_{0,i}}^{T} \frac{\left[\Delta \widetilde{D}_{i,t}^{\text{Data}} - (1+d_i)\sum_{j=1}^{\mathcal{J}} w_{i,j}\, f_{i,j}\left(t - t_{0,i} - c_{i,j}\right)\right]^2}{2\sigma_{i,k_t}^2},
\end{aligned} \tag{7}$$

$$\begin{aligned}
&\mathcal{L}\left(\Delta \widetilde{D}_{i,t}^{\text{Data}} \mid \Delta \widetilde{D}_i^{t-1,\,\text{Data}}, \theta_i\right) = \\
&\qquad \sum_{k_t=1}^{\mathcal{K}} \left[\mathcal{L}\left(\Delta \widetilde{D}_{i,t}^{\text{Data}} \mid \Delta \widetilde{D}_i^{t-1,\,\text{Data}},\, k_t,\, \theta_i\right) p\left(k_t \mid \Delta \widetilde{D}_i^{t-1,\,\text{Data}}, \theta_i\right)\right].
\end{aligned} \tag{8}$$

Given the initial condition $p\left(k_{t_{0,i}-1} \mid \Delta \widetilde{D}_i^{t_{0,i}-1,\,\text{Data}}, \theta_i\right) = 1/\mathcal{K}$, the predictive probability of regime, $p\left(k_t \mid \Delta \widetilde{D}_i^{t-1,\,\text{Data}}, \theta_i\right)$, can be updated recursively through Hamilton (1989)'s filter as

$$p\left(k_t \mid \Delta \widetilde{D}_i^{t-1,\,\text{Data}}, \theta_i\right) = \sum_{k_{t-1}=1}^{\mathcal{K}} q_{k_t,k_{t-1}}\, p\left(k_{t-1} \mid \Delta \widetilde{D}_i^{t-1,\,\text{Data}}, \theta_i\right)$$

and

[13] To offer an accurate account of health consequences of the pandemic, we set $t_{i,0}$ at the time when the number of deaths accumulates to 25 for each location $i$. Our extensive computation confirms that the estimation results reported in this paper are insensitive to whether the cutoff number is 25, 50, or 100.

$$p\left(k_t \mid \Delta\widetilde{D}_i^{t,\,\text{Data}},\, \theta_i\right) = \frac{\mathcal{L}\left(\Delta\widetilde{D}_{i,t}^{\text{Data}} \mid \Delta\widetilde{D}_i^{t-1,\,\text{Data}}, k_t, \theta_i\right) p\left(k_t \mid \Delta\widetilde{D}_i^{t-1,\,\text{Data}}, \theta_i\right)}{\sum_{k_t=1}^{\mathcal{K}} \left[\mathcal{L}\left(\Delta\widetilde{D}_{i,t}^{\text{Data}} \mid \Delta\widetilde{D}_i^{t-1,\,\text{Data}}, k_t,\, \theta_i\right) p\left(k_t \mid \Delta\widetilde{D}_i^{t-1,\,\text{Data}},\, \theta_i\right)\right]}.$$

It follows from equations (7) and (8) that the likelihood function for $\Delta D^{\text{Data}}$ is

$$\mathcal{L}\left(\Delta\widetilde{D}_i^{\text{Data}} \mid \theta_i\right) = \prod_{t=t_{i,0}}^{T} \mathcal{L}\left(\Delta\widetilde{D}_{i,t}^{\text{Data}} \mid \Delta\widetilde{D}_i^{t-1,\,\text{Data}}, \theta_i\right). \tag{9}$$

## 4.2 The Bayesian procedure for estimation

To be agnostic about the values of $\theta_i$, we specify a diffuse prior for $\theta_i$. The prior hyperparameters for each element of $\theta_i$ are determined as described by Liu et al. (2013). First, a wide range of values is selected, and then the hyperparameter values of the prior are chosen such that the 95 percent probability interval covers this wide range. For $a_i$, the Gamma distribution is used with the two hyperparameters set at 1.86 and 0.03, such that the 95 percent prior probability interval is [6.7, 177.7]. For both $b_i$ and $q_i$, the Gamma distribution is used with the two hyperparameters set at 2.44 and 0.54, such that the 95 percent prior probability interval is [0.7, 11.7]. For $c_i$, the normal distribution is used with mean zero and standard deviation 80, such that the 95 percent prior probability interval is $[-157, 157]$. For $d_i$, the Gamma distribution is used with the two hyperparameters set at 1 and 3, such that the 95 percent prior probability interval is [0.0085, 1.2]. For $\sigma_{i,k_t}$, the uniform distribution between 0 and 0.1 is applied.[14] For the weight parameter $w_{i,j}$ $(j = 1, \cdots, \mathcal{J})$ and the elements of $\mathcal{Q}_k$, we use the Beta distribution with the two hyperparameters set at 2 and 2, so

[14]The linear regression literature applies the inverse Gamma distribution to $\sigma_{i,k_t}$ for the purpose of keeping the prior conjugate. For our nonlinear regression here, the inverse Gamma prior is no longer conjugate. Moreover, since the death data implies that the values of $\sigma_{i,k_t}$ are far less than one, the inverse Gamma prior only with no moments can cover such small values. This makes the inverse Gamma prior not only undesirable but also impractical.

that the 95 percent prior probability interval is [0.09, 0.9].[15] All these specifications enable our model parameters to have a broad range, which provides greater flexibility for accounting for the variability and complexity of the underlying density functions in the data. In the Supplemental Appendix provided by Atkeson et al. (2023), we report posterior estimates that are largely within the wide range of our prior. We refer to this component of the prior probability density as $p_1(\theta_i)$.

We impose another component of the prior probability density as

$$p_2(\theta_i) \propto \exp\left\{-\frac{\mathfrak{s}_i}{T-t_{0,i}}\sum_{t=t_{0,i}}^{T}\left[D_{i,t}^{\text{Data}}-\sum_{s=t_{0,i}}^{t}\left[\sum_{j=1}^{\mathcal{J}} w_{i,j}\, f_{i,j}\,(t-t_{0,i}-c_{i,j})\right](1+d_i)D_{i,T}^{\text{Data}}\right]^2\right\},$$

where the hyperparameter $\mathfrak{s}_i$ is set to $10,000$ for most locations for $\log p_2(\theta_i)$. This hyperparameter value is chosen to be on a scale similar to $\log p_1(\theta_i)$. This component of the prior helps minimize the distance between estimated and actual cumulative deaths. It follows that the log posterior density function of $\theta_i$ is

$$\log p\left(\theta_i \mid \Delta\widetilde{D}_i^{\text{Data}}\right) \propto \log \mathcal{L}\left(\Delta\widetilde{D}_i^{\text{Data}} \mid \theta_i\right) + \log p_1(\theta_i) + \log p_2(\theta_i)\,, \tag{10}$$

where $\mathcal{L}\left(\Delta\widetilde{D}_i^{\text{Data}} \mid \theta_i\right)$ is the likelihood function expressed in equation (9).

To find the estimate of $\theta_i$ that maximize the posterior density function represented in equation (10), we begin with thousands of sets of initial parameter values randomly drawn from $p_1(\theta_i)$, and for each set of initial parameter values we use a combination of a constrained optimization algorithm and a hill-climbing quasi-Newton optimization routine to find a local peak. We use this initial local peak to run Markov chain Monte Carlo (MCMC) simulations, and then use these MCMC draws as different starting points for our optimization routine to find a potentially higher peak. We iterate this process until it converges. The global peak has the highest value among all local peaks found by our optimization routines.

[15]Given the expensive computation, we keep the number of states to $\mathcal{K} = 2$ for the volatility parameter governing the regression residual. Increasing the number of states beyond two does not change the results materially while increasing computational burdens drastically.

To obtain the posterior probability distribution of $\theta_i$ for all 132 locations, we use the sequential Monte Carlo method proposed by Waggoner et al. (2016) with C++ software. The locations include 47 states in the United States, the remaining part of the United States, and 86 countries in the rest of the world, as listed in Appendix X.1. The use of the sequential Monte Carlo method and the large number of posterior draws ensure that our results are robust and reliable. The inclusion of all 132 locations enables us to provide a comprehensive analysis of death dynamics caused by the pandemic, as reported in the Supplemental Appendix provided by Atkeson et al. (2023).

The computational cost is high, with each location requiring approximately 2 hours to find the posterior mode and 8 hours to complete 100,000 posterior draws. To accelerate the speed of estimation, we employ a cluster of six nodes to obtain and store a total of 13.2 million posterior draws.[16] These posterior samples enable us to report, with Matlab software, the uncertainty about the estimated trend of deaths as well as the model parameters.

## 4.3 Model fit

We do not smooth the data with a preset filter but rather estimate the death trend using our Bayesian procedure. For each location $i$, the estimation begins at a locality specific date $t_{0,i}$ at which cumulative deaths first reach 25. The sample size for location $i$ is $T_i$.[17] We report the posterior estimates of model parameters, daily deaths, cumulative deaths, and growth rates of deaths for all 132 locations in the Supplemental Appendix provided by Atkeson et al. (2023). We highlight four cases in this section: New York (Figure 1), California (Figure 2), Italy (Figure 3), and Spain (Figure 4). Daily deaths for these locations display distinctly different patterns (top left chart of each figure). It is clear from these figures that the data are noisy and there are reporting errors. For New York, Italy, and Spain, negative deaths are reported; for Spain, zero deaths are reported for numerous days in the later part of

[16]Each node has 40 cores the speed of 3.5 GHz.

[17]For a given location $i$, $T_i$ represents the total number of days from the initial date $t_{0,i}$ at which cumulative deaths first reached 25 deaths, up to February 2, 2021 when the COVID-19 vaccine became widely available to the general population.

the sample. Despite these noisy data, the model with a mixture of MLL functions has a good fit to the data (first row of each figure). From the estimated daily deaths (top left chart of each figure), we compute (a) the estimated cumulative deaths (top right chart of each figure), and (b) growth rates of estimated daily deaths (second and third rows of each figure). We plot growth rates of actual daily deaths against growth rates of estimated daily deaths (middle left chart of each figure). The growth rate of actual daily deaths is calculated based on a moving 7-day average of daily deaths; otherwise, the growth rates would be even noisier than what is displayed in the middle left chart of each figure.[18] In all four cases, daily death growth rates fell rapidly within the first 30 days, but exhibited substantial fluctuations around zero percent thereafter.

As one can see from these figures, all locations experienced a second wave of high death tolls. In the Supplemental Appendix provided by Atkeson et al. (2023), it is shown that some locations experienced spikes in the growth rate of daily deaths during the sample period or even a third wave of high death tolls. As a technical detail, most of these spikes were short-lived due to the discontinuity of differentiability when one MLL density function transitions to another in the mixture of MLL density functions. Out of the 132 locations studied, only two locations had a second wave of daily deaths with a spike in the growth rate greater than 10 percent that did not fall below 10 percent within 30 days.

# 5 Monte Carlo study with the death data simulated from the SEIRHD model

Extended continuous-time SIR models or SIR-based economic models allow for high-order derivatives with respect to time in the path of deaths. Since epidemiologists and economists use these models to inform policy decisions and interventions, it is important to demonstrate whether our MLL approach can fit well data generated by an underlying process that allows for high-order derivatives of cumulative deaths. By showing that our MLL density function approach can successfully capture the full complexity of the death dynamics, even in data

[18]The actual growth rate at a particular time may not be calculable if the reported number of deaths in the denominator is zero.

sets that have higher-order time derivatives, we provide quantitative results that enable epidemiologists and economists to gain new insights into the behavior of the pandemic.

In this paper, we propose a mixture of MLL density functions for modeling the death data across 132 locations. One limitation of the MLL density function is that it does not have independent high-order time derivatives.[19] To address this limitation, we conduct a Monte Carlo study to examine whether our MLL density approach is capable of fitting a distribution of deaths, simulated from the SEIRHD model, that has high-order derivatives.[20] One reason why higher-order derivatives are relevant in SIR models is that they can capture the complex dynamics of deaths caused by the pandemic. For instance, second-order derivatives help capture changes in the rate of new infections, while higher-order derivatives may reveal more subtle patterns of acceleration or deceleration of infections and the growth of deaths.

We first simulate paths of deaths with two initial growth rates that are significantly different (SEIRHD I and SEIRHD II) and then add random noise to each of these deterministic paths (see Appendix X.2.3 for a detailed description of the simulations). The random noise is sampled from the normal distribution with mean zero and a variance whose value changes over time. We apply our Bayesian estimation procedure described in Section IV to these two simulated paths of daily deaths. We find that the mixture number $\mathcal{J} = 3$ is needed for the SEIRHD I model and $\mathcal{J} = 4$ for SEIRHD II.

Figures 5 and 6 show that our estimation procedure works well in approximating the distribution of daily deaths (top left chart of each figure) and the cumulative deaths (top right chart of each figure). With our estimation results, we extract the trend growth rate from the very noisy growth rates of deaths implied by the simulated data (bottom left chart of each figure). The estimated (trend) path of death growth rates tracks the simulated path of deaths (without simulated random noise) reasonably well (bottom right chart of each figure).

[19] That is, the higher-order derivatives of our MLL density functions are pinned down by the parameters that determine the lower-order derivatives of these functions.

[20] The SEIRHD model is described in Appendix X.2.

We calibrate models SEIRHD I and SEIRHD II so that the initial growth rate of deaths is far apart. One challenging question is whether our estimation procedure, which is independent of structural models, is able to distinguish these two distinct paths of deaths in the initial period. Figure 7 compares the estimated paths for the simulated data from models SEIRHD I and SEIRHD II in the initial 30 days. It is evident from the figure that even after taking into account the parameter uncertainty for the mixture of MLL density functions, our estimation procedure is capable of distinguishing the two death paths simulated from the SEIRHD model.

Overall, our Monte Carlo results suggest that the mixture of MLL density functions is able to fit well to the simulated data, even in the presence of higher-order derivatives. Thus, our MLL approach provides a flexible and scalable framework for capturing the complexity of death dynamics during the pandemic period.

## 6 Interpreting estimation results with an SIR model

We use a baseline SIR epidemiological model to interpret our estimation results for COVID-19 deaths as follows.[21] The population is set to $N$. At each moment of time, the population is divided into four categories (states) that sum to the total population. These states are susceptible $S$, infected $I$, resistant $R$ , and dead $D$. Individuals that are susceptible are at risk of getting the disease. Individuals that are infected are contagious and may pass it on to others through some form of interaction with susceptible individuals. Individuals that are resistant are not at risk of getting the disease, either because they have immunity built up from a vaccine or from previous experience with this or similar diseases. Likewise, those who have died from the disease are no longer at risk of getting the disease. We normalize the total population $N = 1$, so all results regarding $S$, $I$, $R$ and $D$ should be interpreted as fractions of the relevant population.

We use $\mathcal{R}(t)$ to denote the *effective reproduction number* of the disease at date $t$. This effective reproduction number is the ratio of the rate at which infected individuals infect

[21] In Appendix X.2, we consider three extensions of our baseline SIR model.

susceptible individuals to the recovery rate of infected individuals from the disease at date $t$.

The equations of the model can be stated in terms of the effective reproduction number as

$$dS(t)/dt = -\mathcal{R}(t)\gamma I(t), \tag{11}$$

$$dI(t)/dt = (\mathcal{R}(t) - 1)\,\gamma I(t), \tag{12}$$

$$dR(t)/dt = (1 - \nu)\gamma I(t), \tag{13}$$

and

$$dD(t)/dt = \nu\gamma I(t). \tag{14}$$

The parameter $\gamma$ governs the rate at which individuals who are infected stop being infectious and hence stop transmitting the disease. We refer to this parameter as the *recovery rate*. This parameter is considered a fixed parameter determined by the biology of the disease. We denote the fatality rate from the disease by $\nu$.

The parameter $\beta(t)$ is the rate at which infected individuals spread the virus to others that they encounter at date $t$. We refer to this parameter as the *transmission rate*. We define the ratio $\beta(t)/\gamma$ to be the *normalized transmission rate*. It is standard to refer to the value of the normalized transmission rate at the start of the pandemic before any mitigation measures and use of prophylactics are undertaken as the *basic reproduction number* of the disease. We denote this basic reproduction number by $\mathcal{R}_0 \equiv \beta(0)/\gamma$.

We assume that infected individuals interact randomly with other individuals in a uniform manner so that the effective reproduction number of the disease is given by the product of the normalized transmission rate and the fraction of individuals who remain susceptible to the disease:

$$\mathcal{R}(t) = \frac{\beta(t)}{\gamma}\frac{S(t)}{1 - D(t)}. \tag{15}$$

We see from equation (15) that the effective reproduction number can fall either due to changes in the normalized transmission rate or changes in the fraction of the population remaining susceptible to the disease.

To invert this model to interpret data on deaths note that from (14), we have

$$I(t) = \frac{1}{\nu\gamma} dD(t)/dt. \tag{16}$$

Using (13) and (14) together and the assumption that $R(0) = D(0) = 0$, we have that

$$R(t) = \frac{1 - \nu}{\nu} D(t). \tag{17}$$

Using that the states must sum to one, we have

$$S(t) = 1 - \frac{1}{\nu} D(t) - \frac{1}{\nu\gamma}\frac{dD(t)}{dt}. \tag{18}$$

To obtain the effective reproduction number implied by deaths data, note that from equations (12) and (16), and the time derivative of equation (16), we have

$$\mathcal{R}(t) = 1 + \frac{1}{\gamma}\frac{\frac{d^2 D(t)}{dt^2}}{\frac{dD(t)}{dt}}, \tag{19}$$

where the last term in this equation can be interpreted as the time derivative of the logarithm of daily deaths.

Equation (19) implies that there is a linear relationship between the growth rate of daily deaths (here measured as the time derivative to the logarithm of daily deaths) and the model-implied effective reproduction number. This reproduction number is equal to one when the growth rate of daily deaths is equal to zero. The slope of this relationship is given by $1/\gamma$ corresponding to the number of days on average that an infected individual remains infectious. To compute estimates of the effective reproductive number that are consistent with our estimated paths for the growth rate of daily deaths, we set $\gamma = 0.2$. This value

implies that if the growth rate of daily deaths is 30 percent initially, the basic reproduction number, the value of the effective number at date $t = 0$, is 2.5. These values are inline with estimates from the Centers for Disease Control and Prevention (CDC).

Given these equations, one can obtain an estimate of the normalized transmission rate of the disease from equations (15) and (18). Thus, one can use this estimate to determine the extent to which the model-implied effective reproduction number has changed due to changes in the transmission rate versus a reduction in the fraction of the population remaining susceptible to the disease. For this exercise we also need to set a value for $\nu$. We use the CDC's preferred estimate of this parameter and set $\nu = 0.004$.

## 7 Four stylized facts

While the above structural interpretation connects the number of deaths to the effective reproduction number, our estimation results discussed in Section IV do not depend on any structural model. In addition to those results, our estimation yields the following four stylized facts about the COVID-19 pandemic.

**Fact 1.** *The growth rate of daily deaths from COVID-19 fell rapidly within the first 30 days after each location in our sample reached 25 cumulative deaths.*

Fact 1 is depicted in the top chart of Figure 8. The estimated growth rate of daily deaths, with 0.68 and 0.95 posterior probability intervals, declined rapidly within the first 30 days of the estimation period from a wide range of initial high levels to low levels around zero percent. The posterior probability bands account for both location and sampling uncertainty, with most cross-location dispersion driven by location uncertainty (bottom chart of Figure 8). Sampling uncertainty within a location is small.

**Fact 2.** *After the initial 30-day period of rapid decline, daily death growth rates in all locations in our sample exhibit substantial fluctuations around zero percent.*

Despite the heterogeneity in both their geographic locations and daily death patterns, all locations in the sample showed fluctuations around zero percent (-5 percent to 10 percent) after the initial 30-day period (bottom chart of Figure 8). In all four of our example locations

(middle and bottom charts of Figures 1–4), the growth rate of daily deaths followed a path consistent with Facts 1 and 2.

**Fact 3.** *The dispersion of growth rates of deaths across locations decreased rapidly in the first 10 days of the pandemic, but remained substantial thereafter.*

Fact 3 can also be seen in Figure 8. The shrinking of the 0.68 and 0.95 posterior probability intervals shows that the dispersion in death growth rates across locations decreased sharply within the initial 10 days of the pandemic.

Table 1 presents numerical values for Facts 1–3.[22] Taken together, Figure 8 and Table 1 demonstrate important differences in the evolution of daily death growth rates early on versus later on in the COVID-19 pandemic. In particular, these facts indicate that there was a structural break in the impact of COVID-19 on deaths occurring roughly 30 days after 25 cumulative deaths occurred. Prior to the structural break is a period characterized by rapidly declining growth rates of daily deaths and high cross-location dispersion. The period after the structural break shows significantly less cross-location dispersion in death growth rates compared to the early period, but still exhibits substantial fluctuations across locations.

**Fact 4.** *When interpreted through a range of epidemiological models, Facts 1–3 imply that both effective reproduction numbers and transmission rates of COVID-19 fell rapidly from widely dispersed initial levels during the first 30 days after cumulative deaths reached 25. After this initial period of rapid decline, the effective reproduction number hovered around one almost everywhere in the world.*

Fact 4 is obtained by deriving the implications of our estimated daily death paths for the paths of effective reproduction numbers and transmission rates using four variants of the SIR model. The baseline version is described in Section VI, and the effective reproduction

[22] We report the maximum and minimum values in the table to reflect extreme cases. Some locations did not experience a wave of high death tolls until later periods, and the negative growth rates estimated for these locations with low death tolls are not significant.

number and normalized transmission rates implied by this model are obtained from the deaths data using equations (15), (18), and (19). The parameter $\gamma$ is set to 0.2 such that a growth rate of daily deaths of 30 percent corresponds to a basic reproduction number of 2.5. The left chart of Figure 9 shows that the median effective reproduction number fell from an initial level of nearly 3 to 1 in 30 days and subsequently remained slightly below 1.

Equation (15) illustrates that the effective reproduction number can fall because of both declines in the normalized transmission rate and declines in the fraction of the population remaining susceptible to the disease. We use our estimated paths for daily deaths and the equations of the baseline SIR model to determine the relative contributions of each. We find that the rapid decline in daily death growth rates early on in the pandemic is primarily due to a rapid fall in the transmission rate of the disease. Disease transmission rates, like effective reproduction numbers, fell early on in the pandemic from widely dispersed initial levels and remained low after the initial period.

To explore the robustness of our results to SIR model uncertainty, we consider three variants of the baseline SIR model: an SEIRD model which extends the SIR model by assuming individuals first become exposed to the disease before becoming infectious, an SIHRD model which allows for a longer period between infection and death by adding a hospitalized state, and an SEIHRD model which extends the SIR model by adding both the exposed state and the hospitalized state. Following a similar procedure as with the baseline SIR model, we are able to express the effective reproduction number as a function of model parameters, as well as, daily deaths and its derivatives for each model extension.[23] For each posterior draw of the parameter set consisting of $a_{i,j}$, $b_{i,j}$, $q_{i,j}$, $c_{i,j}$, $d_{i,j}$, and $w_{i,j}$, we invert the four structural SIR models to obtain the effective reproduction number and the transmission rate. This computation is extremely expensive if the number of mixture functions is greater than one. For a mixture of two MLL density functions, for instance, it takes at least two hours for each location to solve each structural SIR model with 1,000 posterior draws.

Figure 9 shows that our findings are robust to variations of the baseline SIR model. The left chart of the figure shows that, across all four model variations, estimated effective

[23]Details on these model extensions are provided in Appendix X.2.

reproduction numbers fell rapidly in the first period before the structural break.[24] In the second period after the structural break, the median effective reproduction numbers implied by each model, hover slightly below 1. The structural break we discuss here is conceptual as the purpose of this paper is *not* to define a strictly econometric breakpoint. We use the first 30 days as an illustration to show that the characteristics of death growth rates and effective reproduction numbers change, *qualitatively*, from a period prior to the structural break to a period after, whenever a large spike of death growth rates occurs during a first, second, or third wave of rapidly rising deaths.

No matter how one defines when the structural break occurs, it is unambiguous that the initial period is characterized by more cross-location and cross-model dispersion in effective reproduction numbers than the later period of the sample. The right chart of Figure 9 shows that, regardless of model, the cross-location standard deviation of effective reproduction numbers fell substantially within the first 10 days of the estimation period and, subsequently, remained stable and relatively low.

## 8 Discussion of alternative estimation methods

In previous sections, we discuss the challenges of developing an estimation procedure for fitting daily deaths and their growth rates to noisy data. In this section, we evaluate three alternative methods for tackling this challenging task: the HP filter, the local linear trend (LLT) method (Madsen, 2007, Chapter 3), and the non-parametric monotone function (NPMF) estimation method (Shively et al., 2009).

### 8.1 The HP filter

We apply the HP filter to estimation of of daily deaths with various values of the smoothing parameter: 50, 200, 1600, 14400, and 144000. The standard value is 1600 for quarterly data and 14400 for monthly data. If scaled to daily data, the value is 12960000. With values too

[24] Although we do not report transmission rates here, they fell rapidly in the initial period as well regardless of SIR model.

large or small, the HP filter fits poorly. The best smoothing value appears to be 200, used by Fernandez-Villaverde and Jones (2020).

The use of the smoothing parameter in the HP filter helps optimize the fit of the death growth rate over a longer period, but this benefit comes at the expense of decreased accuracy in the early stages of the pandemic. This trade-off is demonstrated in Figures 10 and 11, which show the fit to the data from Spain and to the simulated data generated by SEIRHD II. As seen in these figures, while the fit to the death growth rate is reasonable over a longer time horizon, it is poor in the early stages of the pandemic.

## 8.2 The LLT method

The LLT method is a more advanced unobserved component model for estimating daily deaths than the HP filter. It is described in detail in Madsen (2007, Chapter 3). The objective is to estimate a $2 \times 1$ vector of parameters, represented by $\boldsymbol{\theta} = \begin{pmatrix} \theta_0 & \theta_1 \end{pmatrix}'$, such that

$$\hat{\boldsymbol{\theta}}_T = \arg\min_{\boldsymbol{\theta}} S(\boldsymbol{\theta}; T), \tag{20}$$

where

$$S(\boldsymbol{\theta}; T) = \sum_{t=0}^{T-1} \lambda^t \left[ d_{T-t} - (\theta_0 - t\theta_1) \right]^2,$$

$\boldsymbol{d} = \begin{pmatrix} d_1 & d_2 & \cdots & d_T \end{pmatrix}'$ is a vector of the observed daily deaths, and $\lambda$ is the forgetting factor. The weighted least squares solution to (20) is

$$\hat{\boldsymbol{\theta}}_T = \left( \boldsymbol{x}_T' \boldsymbol{\Sigma}^{-1} \boldsymbol{x}_T \right)^{-1} \boldsymbol{x}_T' \boldsymbol{\Sigma}^{-1} \boldsymbol{d},$$

where

$$\boldsymbol{\Sigma} = \operatorname{diag} \left[ \frac{1}{\lambda^{T-1}}, \cdots, \frac{1}{\lambda}, 1 \right],$$

and

$$\boldsymbol{x}_T = \begin{bmatrix} d_1 - (\theta_0 + (1-T)\theta_1) \\ d_2 - (\theta_0 + (2-T)\theta_1) \\ \vdots \\ y_T - \theta_0 \end{bmatrix}.$$

We apply the LLT method to the estimation of daily deaths using both observed data and simulated data from SIR models. Unlike the HP filter, the LLT method lacks a smoothing parameter, but includes a forgetting factor. This factor enhances the accuracy of the death growth rate in the early stages of the pandemic, but can cause excessive fluctuations over a longer time horizon. This trade-off is demonstrated in the figures showing the fit to Spain (Figure 12) and the simulated data generated by SEIRHD II (Figure 13). The results displayed in these figures are calculated using a forgetting factor of $\lambda = 0.9$. The trade-off remains for different values of the forgetting factor.

## 8.3 The NPMF method

There is a strand of literature on Bayesian estimation of monotone functions, including Shively et al. (2009) and Bornkamp and Ickstadt (2009). Our approach aligns with this literature, but instead of modeling cumulative deaths as a monotone function, we focus on utilizing the daily death data, which has previously been overlooked. Our parametric approach not only ensures the boundedness of the death growth rate (the second derivative of cumulative deaths), but also allows us to incorporate the impact of multiple death waves caused by virus variants or other socio-economic factors.

In this section, we apply the NPMF estimation approach of Shively et al. (2009) to our death data. To provide a clear understanding of this approach, we include a self-contained description in this section. Denote cumulative deaths by $F(t)$ and consider the following process of $F(t)$ as

$$F(t) = G(t) + \varepsilon_t \qquad t = 1, 2, \cdots, T, \tag{21}$$

where the $\varepsilon_t$'s are independent, identically distributed and follow a normal distribution $\mathcal{N}(0, \sigma^2)$. Shively et al. (2009) use $\mathcal{N}(0, \sigma^2)$ so that the likelihood and posterior functions can be conveniently computed. The estimated function $G(t)$ is bounded by [0, 1] and takes the following functional form:

$$G(t) = \alpha + \int_0^t \exp\left[\beta + \tau w(x)\right] dx, \tag{22}$$

where $\alpha$, $\beta$, and $\tau$ are parameters, and $w(t)$ is a standardized continuous integrable function with $w(0) = 0$. In our estimation, the observation time $t$ is normalized to be in [0, 1].

One method recommended by Shively et al. (2009) is to utilize a number of quadratic functions to approximate $\int_0^t \exp\left[\beta + \tau w(x)\right] dx$. This approximation works poorly for many locations, even with the number of quadratic functions as large as 100. Another method, discussed in Shively et al. (2009), is to use a step function, $\gamma_m(x)$, to approximate the continuous function $\tau w(x)$:

$$\gamma_m(x) = \tau w\left(\frac{[mx]}{m}\right),$$

where $m$ is the number of nodes in the step function, and $[mx]$ is the greatest integer less than or equal to $mx$. Evenly spaced nodes over $[0, 1]$ are considered so that

$$\gamma_m\left(\frac{1}{m}\right), \gamma_m\left(\frac{2}{m}\right), \cdots, \gamma_m(1)$$

are used to approximate $\tau w(x)$ for $x = \frac{1}{m}, \frac{2}{m}, \cdots, 1$.

Denote $k = [mt]$. When $m$ is large, for $(k-1)/m \leq t < k/m$, $G(t)$ can be approximated by $\hat{G}(t)$:

$$\hat{G}(t) = \alpha + \sum_{j=1}^{k-1} \exp\left[\beta + \gamma_m\left(\frac{j-1}{m}\right)\right] \frac{1}{m} + \exp\left[\beta + \gamma_m\left(\frac{k-1}{m}\right)\right]\left(t - \frac{k-1}{m}\right). \tag{23}$$

In our Bayesian simulation, the cumulative deaths over the observation period are normalized by dividing by the last observed cumulative death value. That is, the maximum value of the observed data is normalized to be one. To get the posterior distributions of the parameters $\alpha$, $\beta$, $\gamma_m\left(\frac{1}{m}\right), \gamma_m\left(\frac{2}{m}\right), \cdots, \gamma_m\left(\frac{m-1}{m}\right)$, and $\sigma^2$, the prior distributions of $\alpha$ and $\beta$ are set to the standard normal distribution $\mathcal{N}(0, 1)$. The prior distributions of $\tau^2$ and

$\sigma^2$ are set to uniform distributions on $(0, 1)$. The prior distribution for $w(t)$ is determined by a Wiener process with variance $\tau^2$. Thus, the variance of each independent increment $\sqrt{m}\left[w\left(\frac{i}{m}\right) - w\left(\frac{i-1}{m}\right)\right]$ is $\tau^2$ for $i = 1, \cdots, m$ (Shively et al., 2009, Section 2.4).

We outline the steps in the estimation procedure as follows:

(1) Choose the number of nodes $m$.

(2) Make prior draws of $\alpha$, $\beta$, $\sigma^2$, and $\tau^2$.

(3) Make prior draws for $\gamma_m\left(\frac{1}{m}\right), \gamma_m\left(\frac{2}{m}\right), \cdots, \gamma_m\left(\frac{m-1}{m}\right)$ from the Wiener process with variance $\tau^2$.

(4) Calculate $k$ for each observation point $t$.

(5) Calculate $\hat{G}(t)$ for each observation point $t$.

(6) Calculate the log likelihood and log posterior values for the observed data.

(7) Make posterior draws using the MCMC method.

We utilize a large number of nodes, 50, for approximating the Wiener process in our estimation. Despite obtaining a good fit for cumulative deaths across all locations, our estimation results yield a poor fit to death growth rates in both the short and long horizons (as seen in Figure 14 for Spain and Figure 15 for the simulated data generated by SEIRHD II). Increasing the number of nodes to 100 does not significantly improve the fit.

To summarize, our contribution to the understanding of the spread of COVID-19 leverages daily death data that has been overlooked in previous literature. Through the application of our new methodology, we estimate the process of daily deaths caused by COVID-19 and discover four stylized facts that reveal the limitations of current epidemiological and economic models.

## 9 Conclusion

This paper introduces a novel empirical method for estimating COVID-19 death growth rates from noisy data for 132 locations worldwide, leading to the establishment of four stylized facts. Our method provides several advantages over existing methods, as we demonstrate in our analysis.

Fact 1—the universal rapid decline in the growth rate of COVID-19 deaths during the early stages of the pandemic—implies that common factors drove the decline across different locations, offering insights into the factors that contributed to the rapid decline.

Facts 2–3 reveal a structural break around 30 days after an initial spike in death growth rates, leading to significant fluctuations in death growth rates around zero percent in subsequent periods. These fluctuations persisted, even as various structural SIR models imply that effective reproduction numbers and transmission rates should remain at a low level.

Our study's stylized facts highlight the limitations of existing models in capturing the dynamics of the pandemic and represent a vital step toward improving epidemiological and economic models. By identifying the limitations of current models and revealing commonalities across different locations, our research provides a basis for developing more accurate and effective models for analyzing pandemic impacts and policymaking. Our findings have significant implications for improving public health responses to pandemics, which can reduce their economic and social costs.

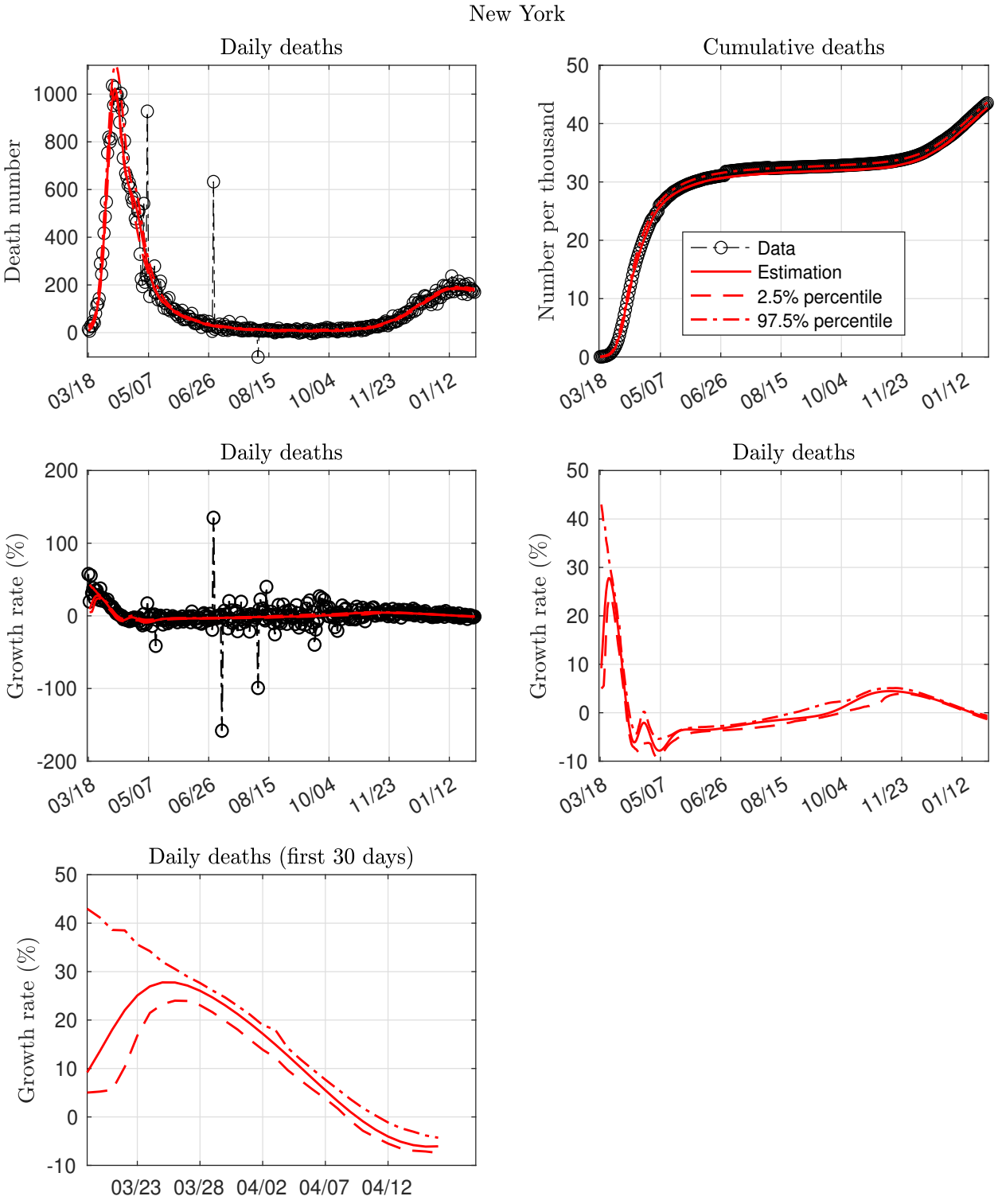


FIGURE 1. New York: Estimates of daily deaths, cumulative deaths, and growth rates from the beginning of the pandemic through February 2, 2021. The estimation is based on the fitted mixture of modified log-logistic density functions. The dash and dash-dotted lines contain 95 percent posterior probability bands for the estimation. The beginning of the pandemic is the earliest date when the cumulative death toll reached 25 in this location.

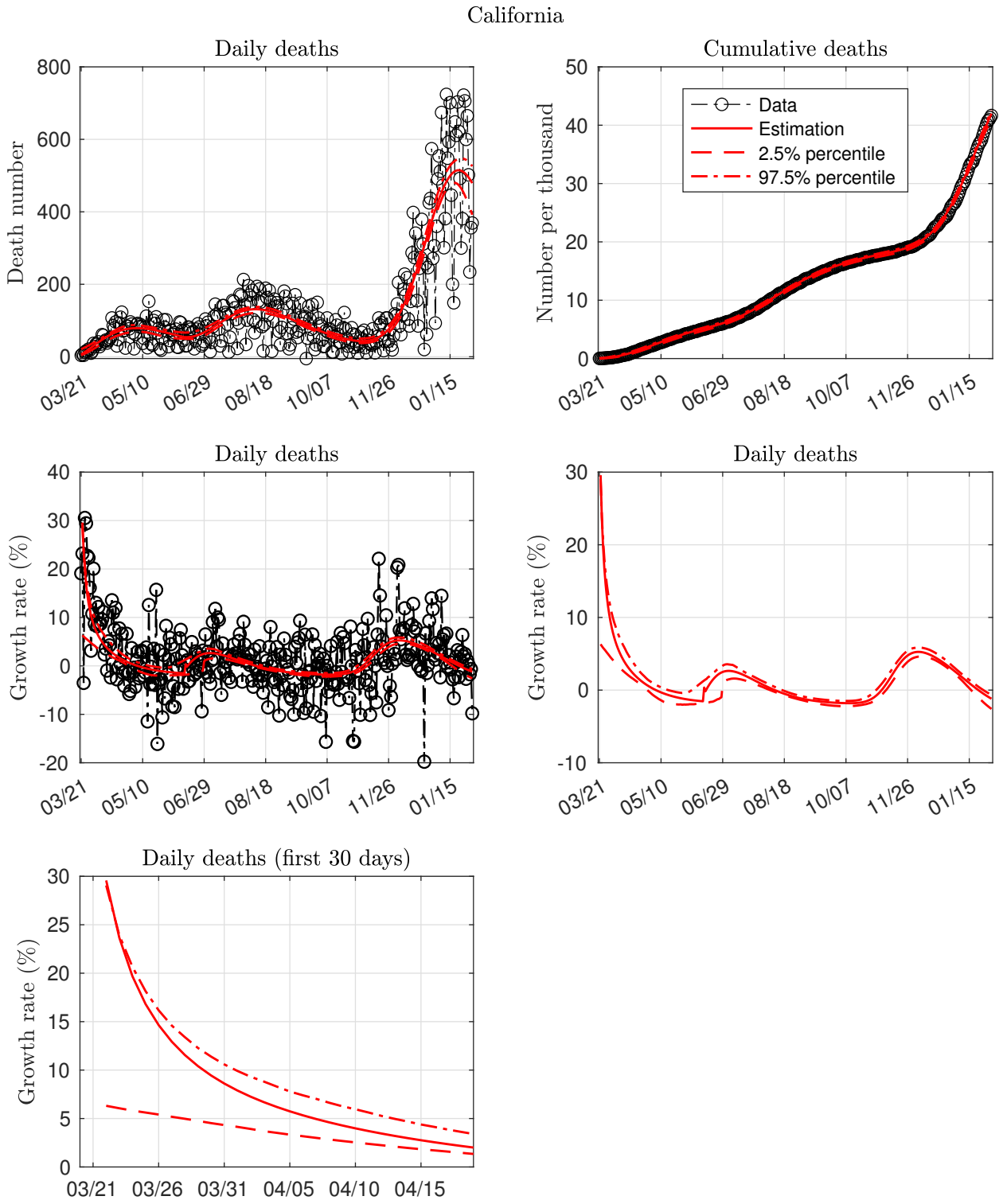


FIGURE 2. California: Estimates of daily deaths, cumulative deaths, and growth rates from the beginning of the pandemic through February 2, 2021. The estimation is based on the fitted mixture of MLL density functions. The dash and dash-dotted lines contain 95 percent posterior probability bands for the estimation. The beginning of the pandemic in this location is the earliest date when the cumulative death toll reached 25.

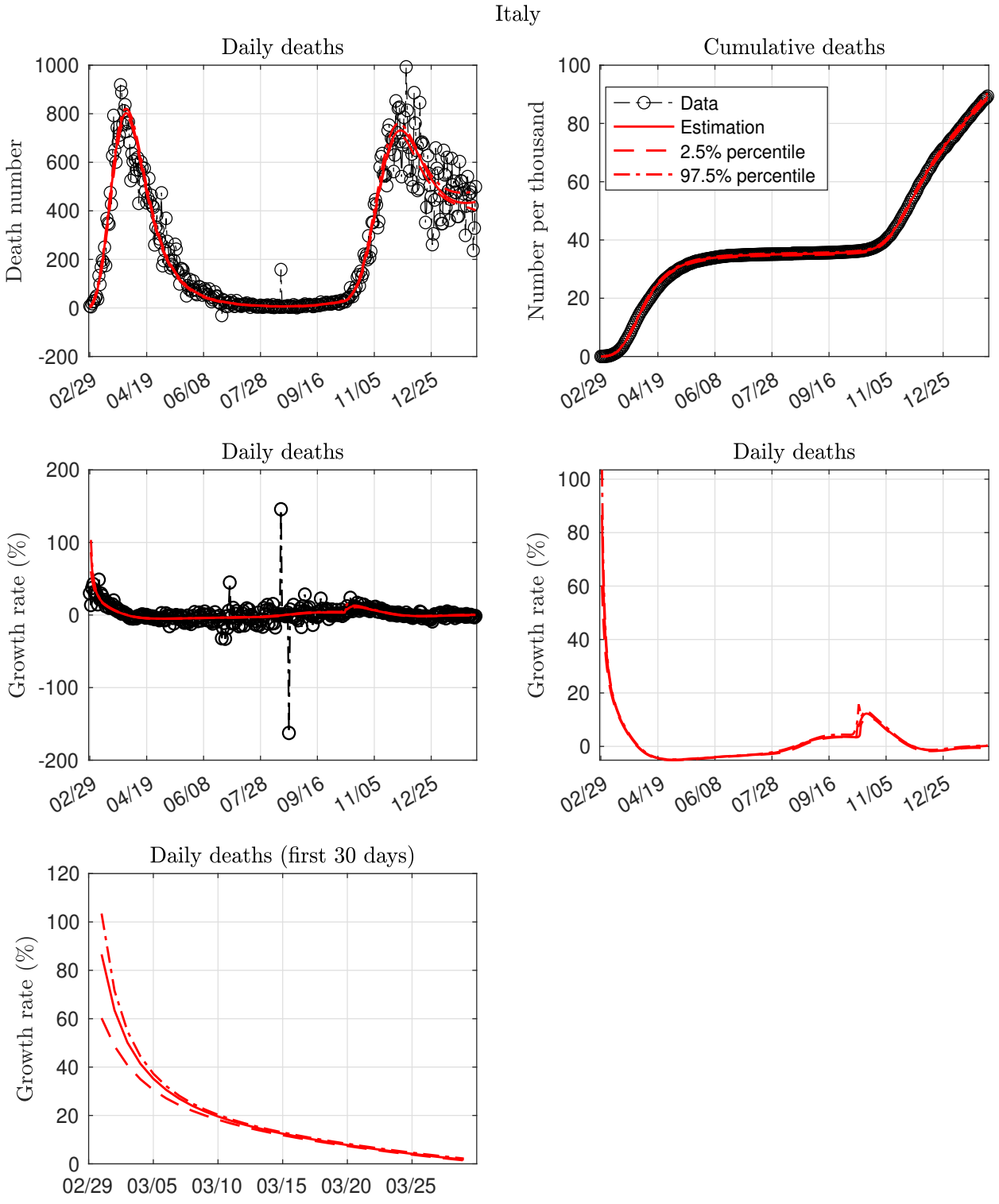


FIGURE 3. Italy: Estimates of daily deaths, cumulative deaths, and growth rates from the beginning of the pandemic through February 2, 2021. The estimation is based on the fitted mixture of MLL density functions. The dash and dash-dotted lines contain 95 percent posterior probability bands for the estimation. The beginning of the pandemic in this location is the earliest date when the cumulative death toll reached 25.

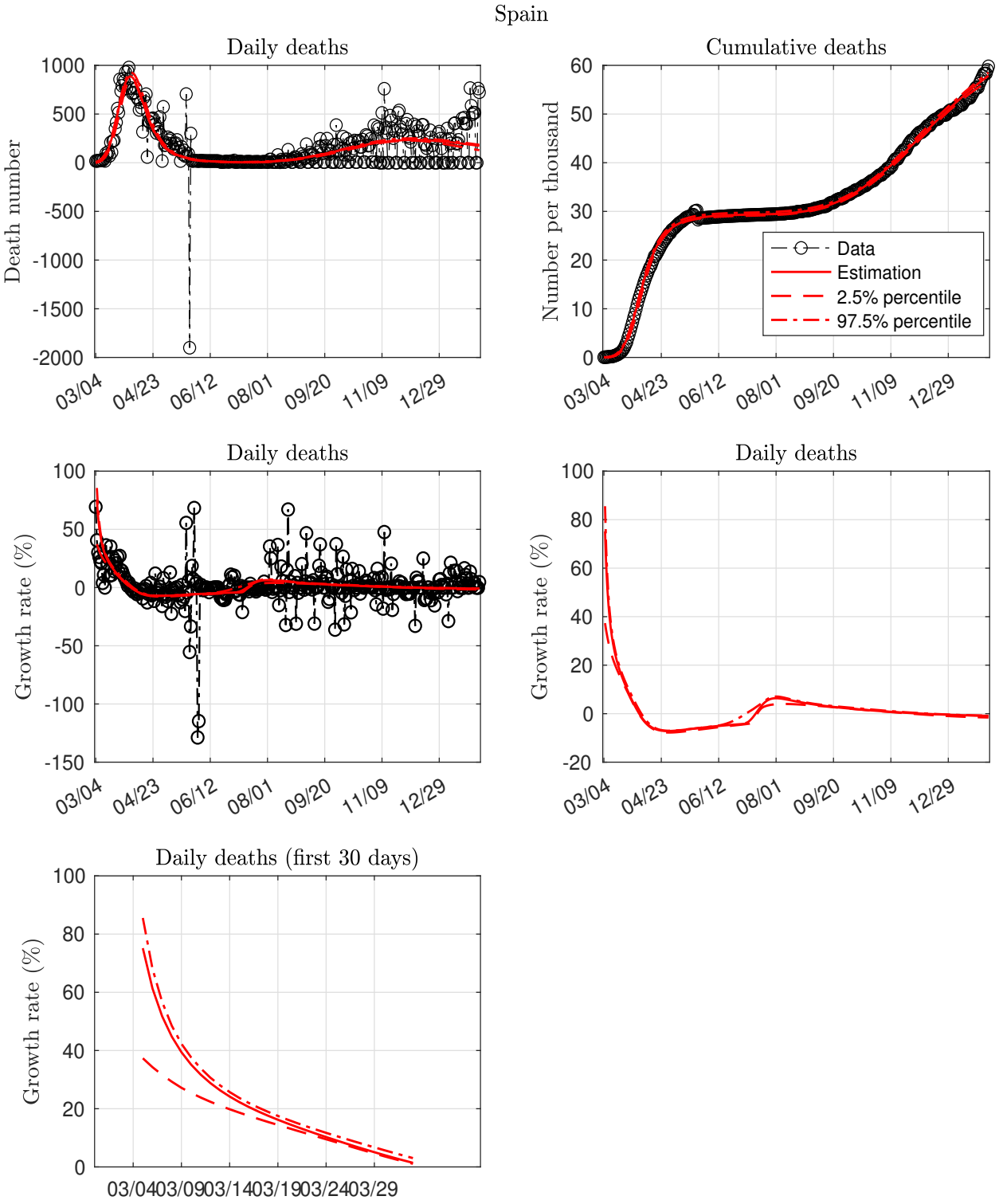


FIGURE 4. Spain: Estimates of daily deaths, cumulative deaths, and growth rates from the beginning of the pandemic through February 2, 2021. The estimation is based on the fitted mixture of MLL density functions. The dash and dash-dotted lines contain 95 percent posterior probability bands for the estimation. The beginning of the pandemic in this location is the earliest date when the cumulative death toll reached 25.

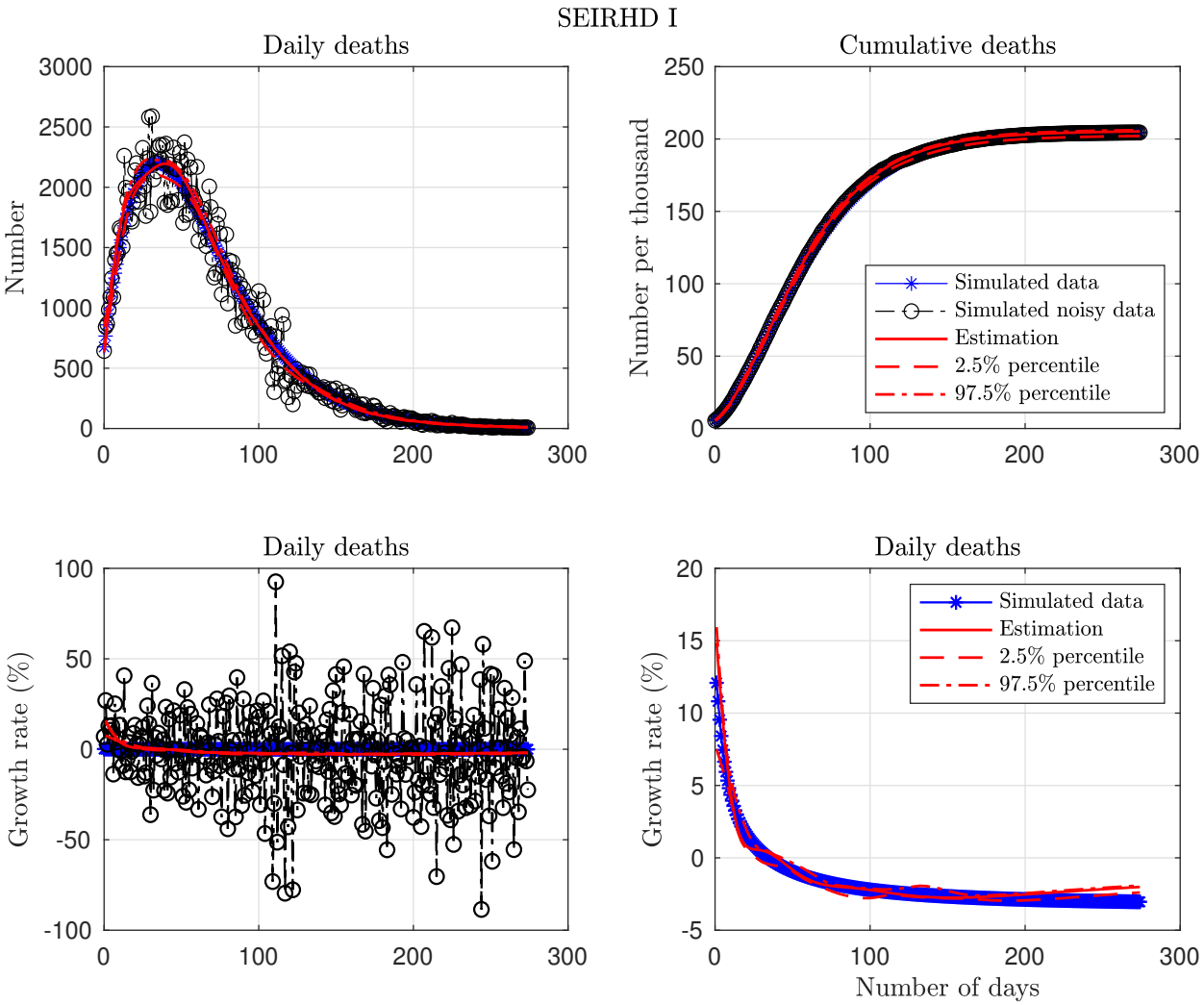


FIGURE 5. Estimation based on artificial death data simulated from theoretical model "SEIRHD I."

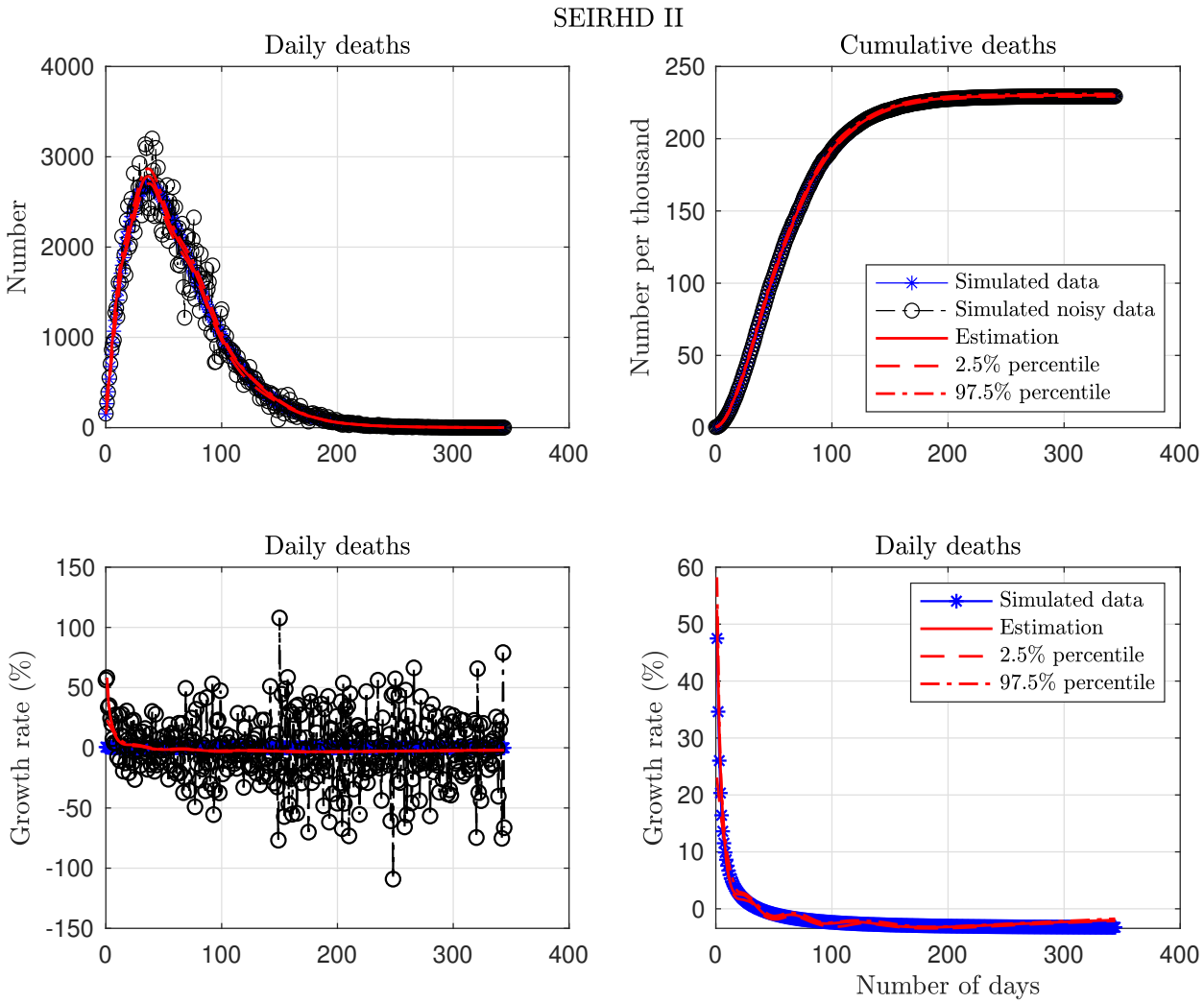


FIGURE 6. Estimation based on artificial death data simulated from theoretical model "SEIRHD II."

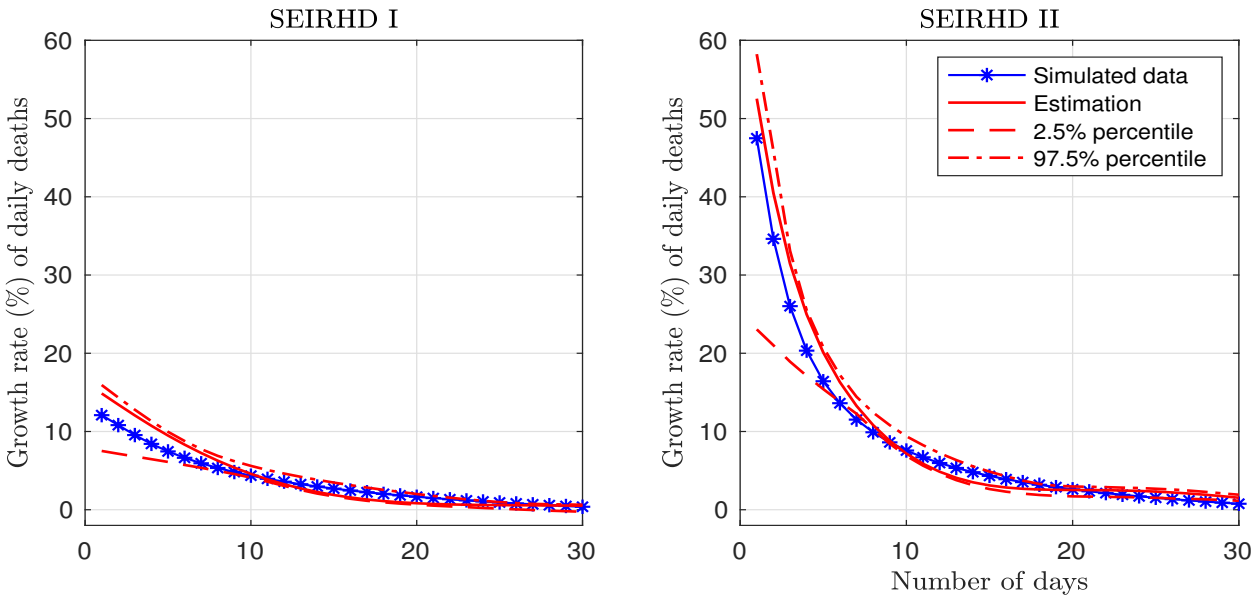


FIGURE 7. First 30 days: Estimation based on the artificial death data simulated from theoretical models "SEIRHD I" and "SEIRHD II."

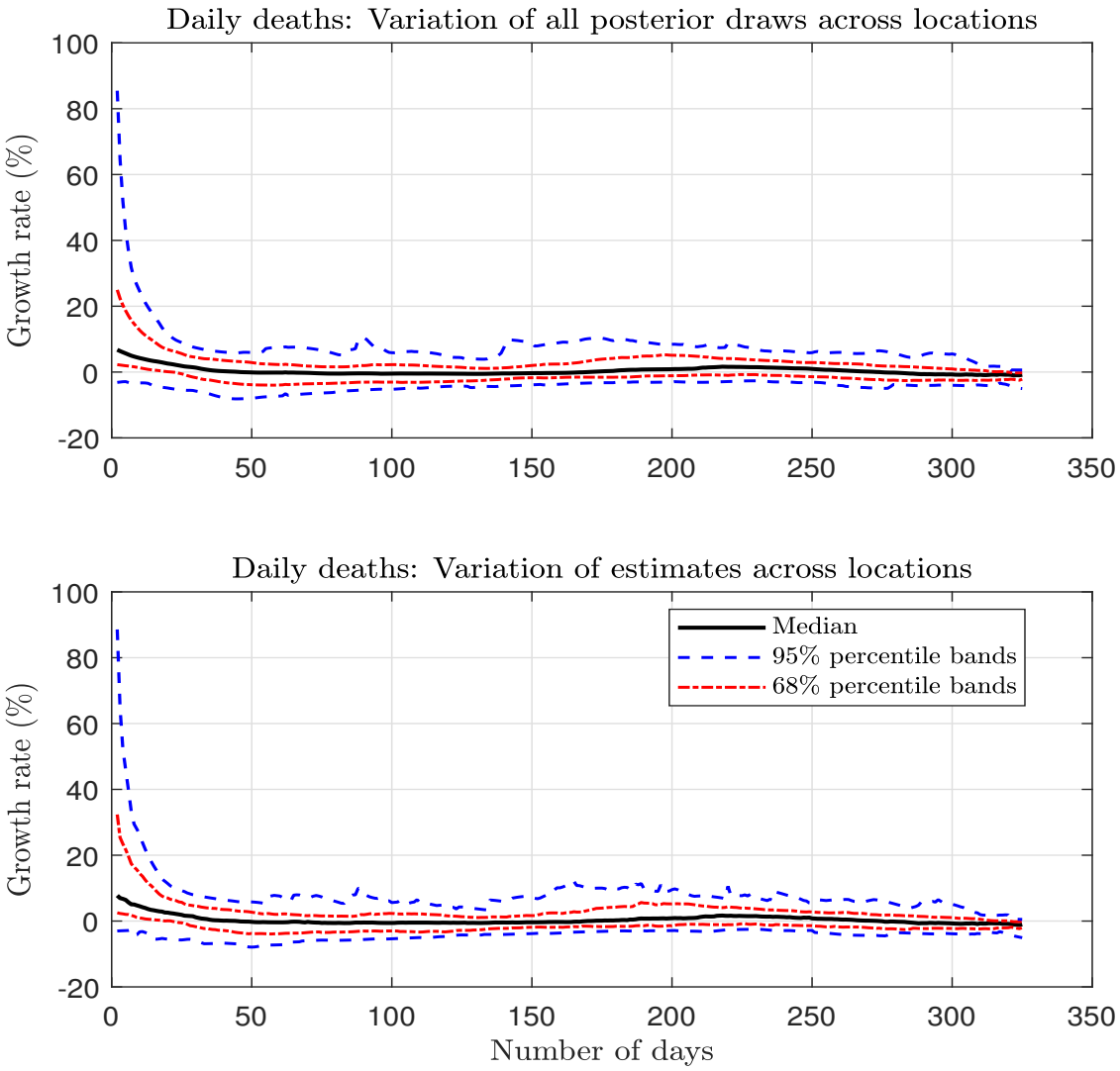


FIGURE 8. Location and sampling uncertainty. The top chart displays the median estimates of death growth rates with both 68 percent and 95 percent posterior probability bands (sampling uncertainty). The bottom chart displays the variation of estimates themselves (with no sampling of model parameters), with the median estimates, 68 percent percentile bands, and 95 percent percentile bands. The bottom chart captures the location uncertainty. The beginning of the pandemic in each location, normalized at Day 1, is the earliest date when the cumulative death toll reached 25.

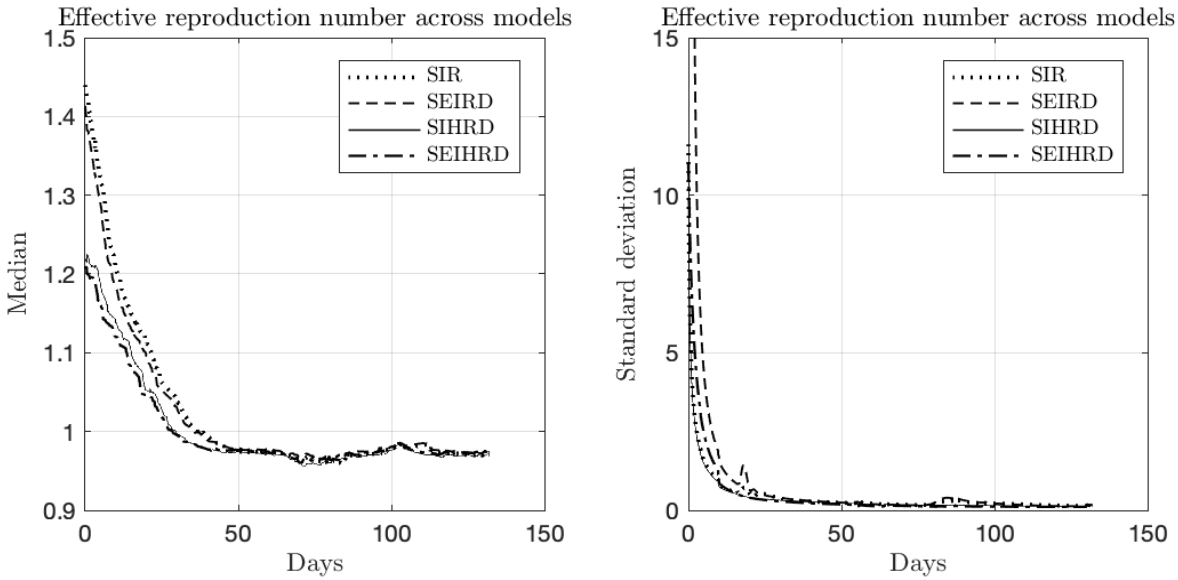


FIGURE 9. SIR model uncertainty: Effective reproduction numbers estimated from the four epidemiological models discussed in the text. The estimated median and standard deviations for each model are based on all 132 locations. Data from different locations imply different parameters for each model. Day 0 in each location is the earliest date when the cumulative death toll reached 25.

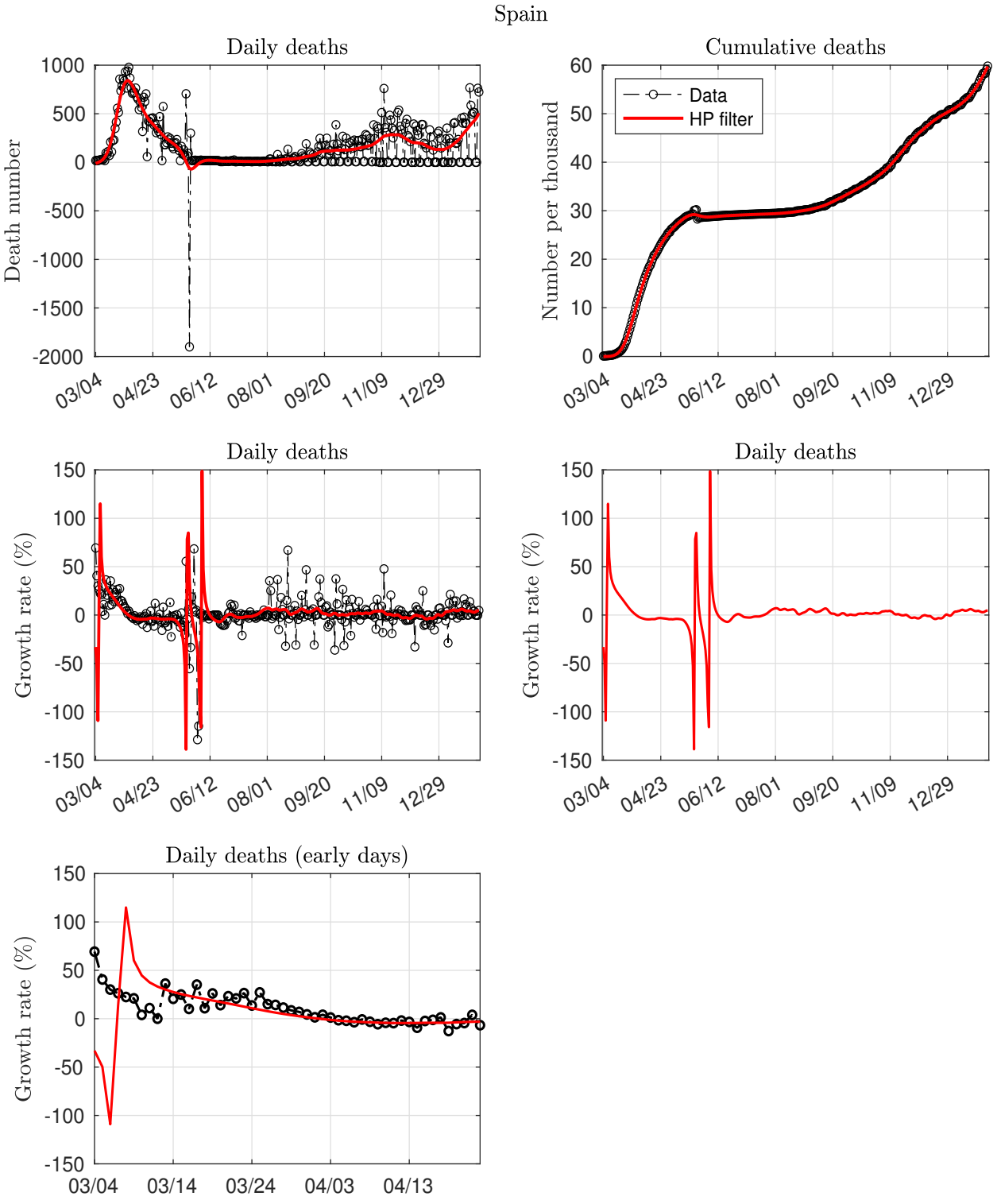


FIGURE 10. Spain: Estimates of daily deaths, cumulative deaths, and growth rates from the beginning of the pandemic through February 2, 2021. The estimation is based on the HP filter. The beginning of the pandemic in this location is the earliest date when the cumulative death toll reached 25.

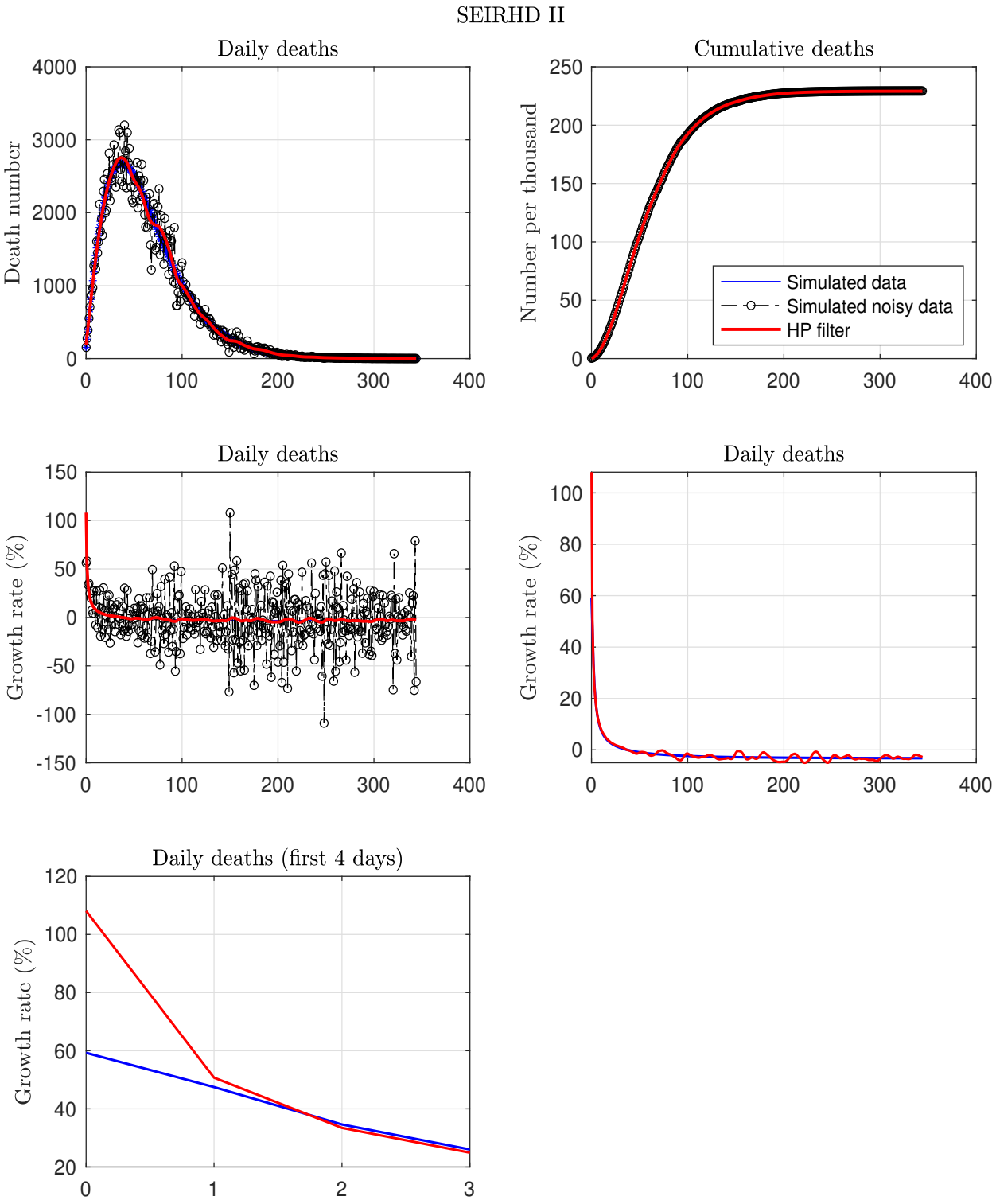


FIGURE 11. Estimation based on the HP filter applied to artificial death data simulated from theoretical model "SEIRHD II."

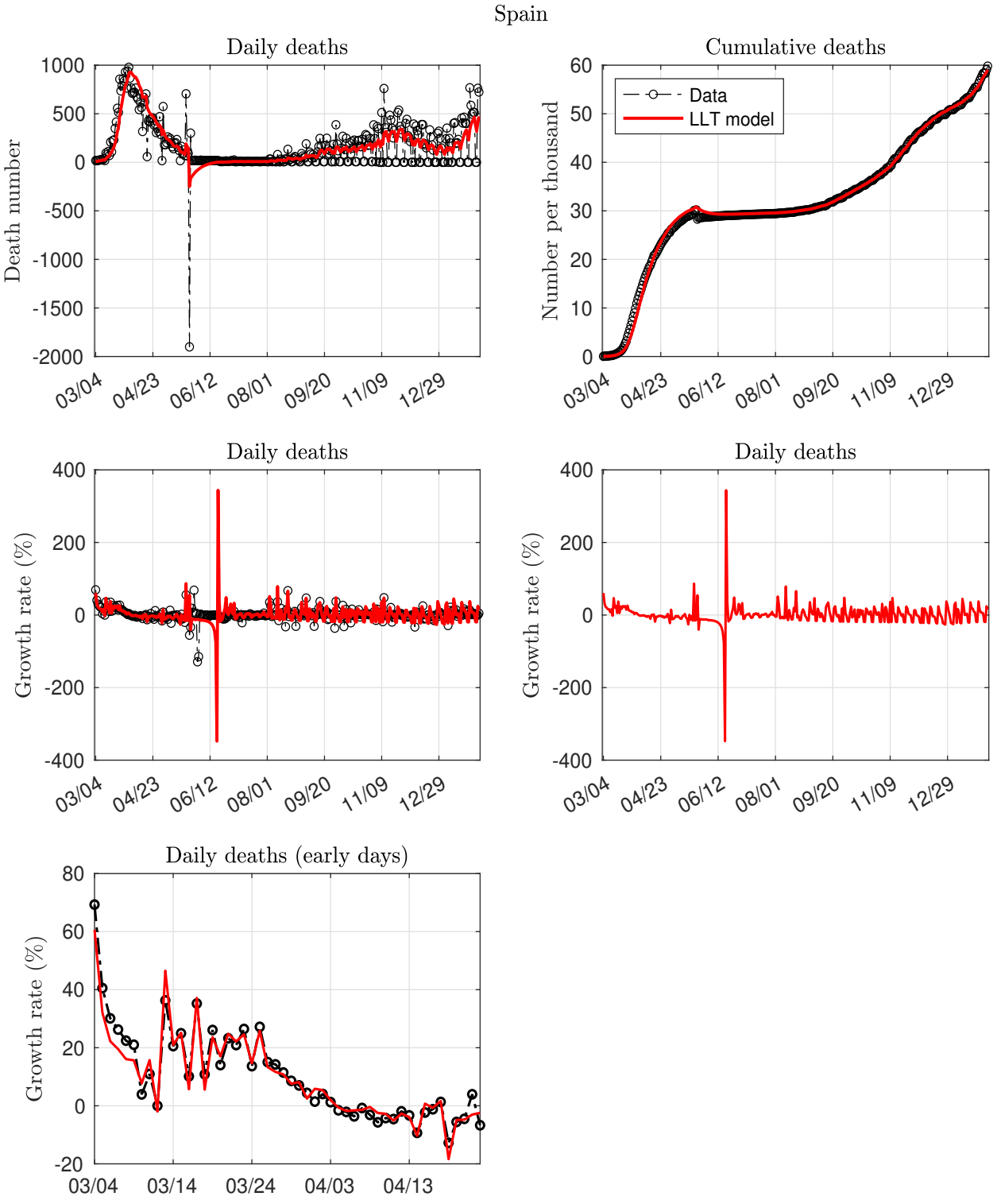


FIGURE 12. Spain: Estimates of daily deaths, cumulative deaths, and growth rates from the beginning of the pandemic through February 2, 2021. The estimation is based on the LLT model. The beginning of the pandemic in this location is the earliest date when the cumulative death toll reached 25.

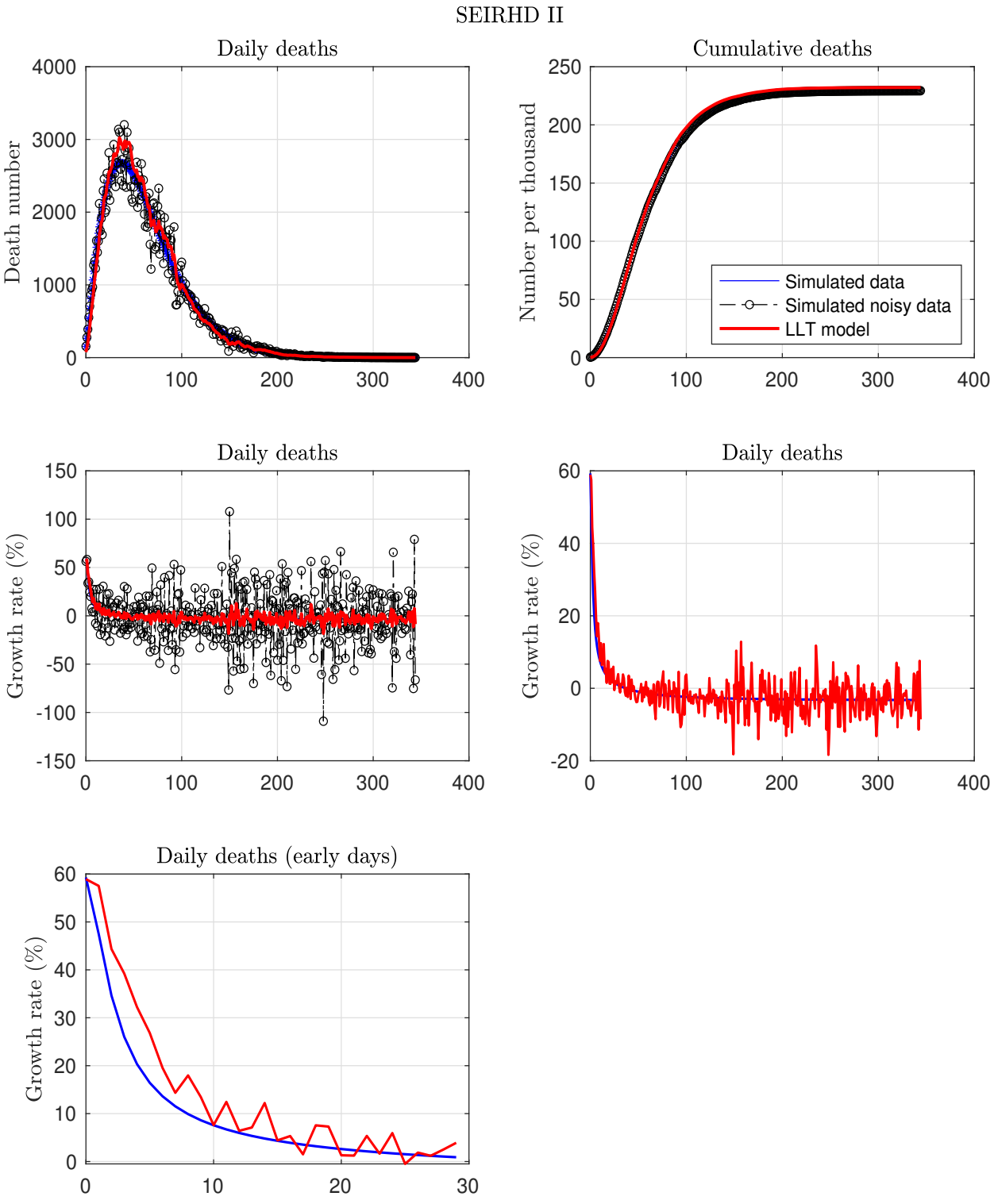


FIGURE 13. Estimation based on the LLP model applied to artificial death data simulated from theoretical model "SEIRHD II."

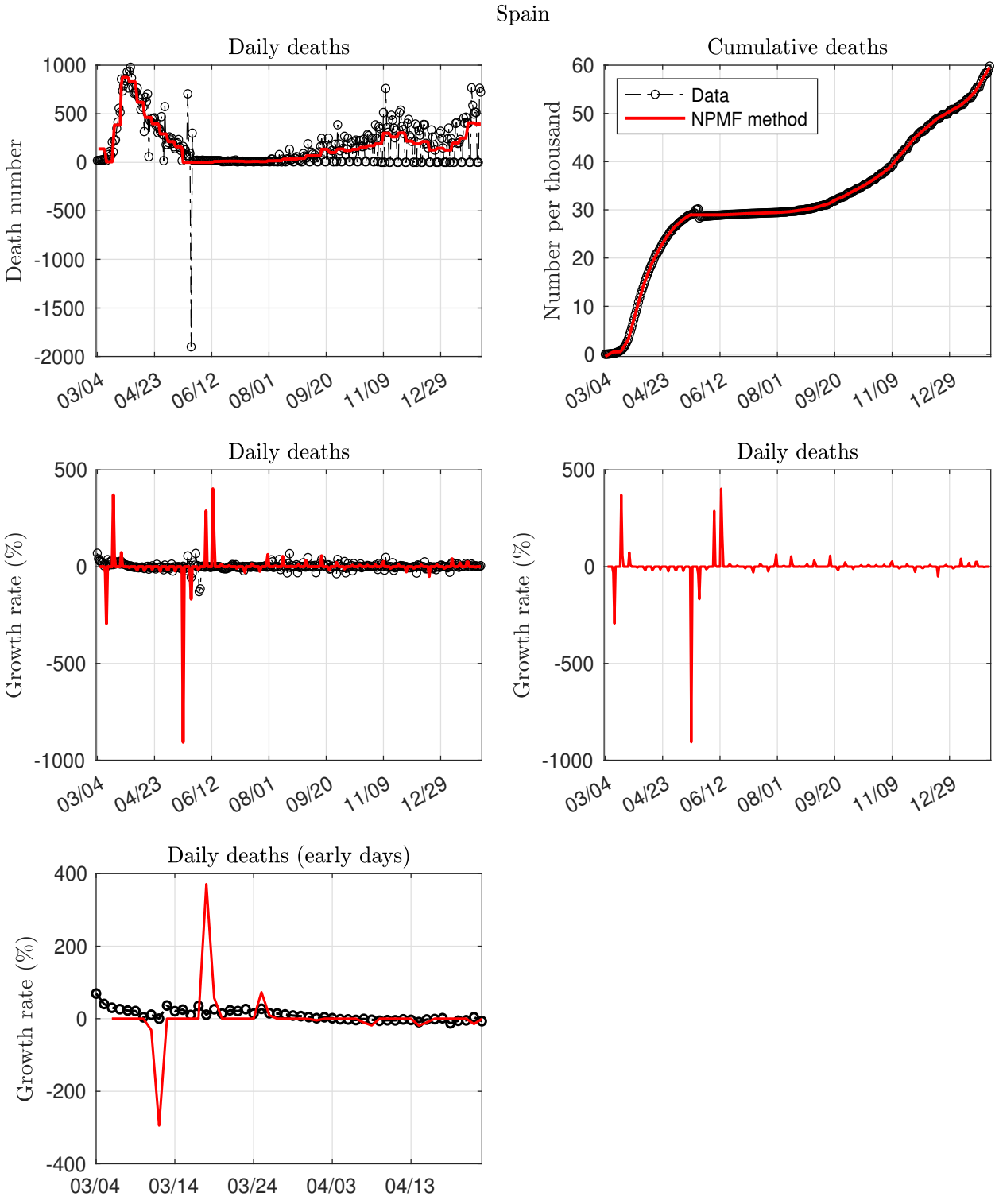


FIGURE 14. Spain: Estimates of daily deaths, cumulative deaths, and growth rates from the beginning of the pandemic through February 2, 2021. The estimation is based on the NPMF method. The beginning of the pandemic in this location is the earliest date when the cumulative death toll reached 25.

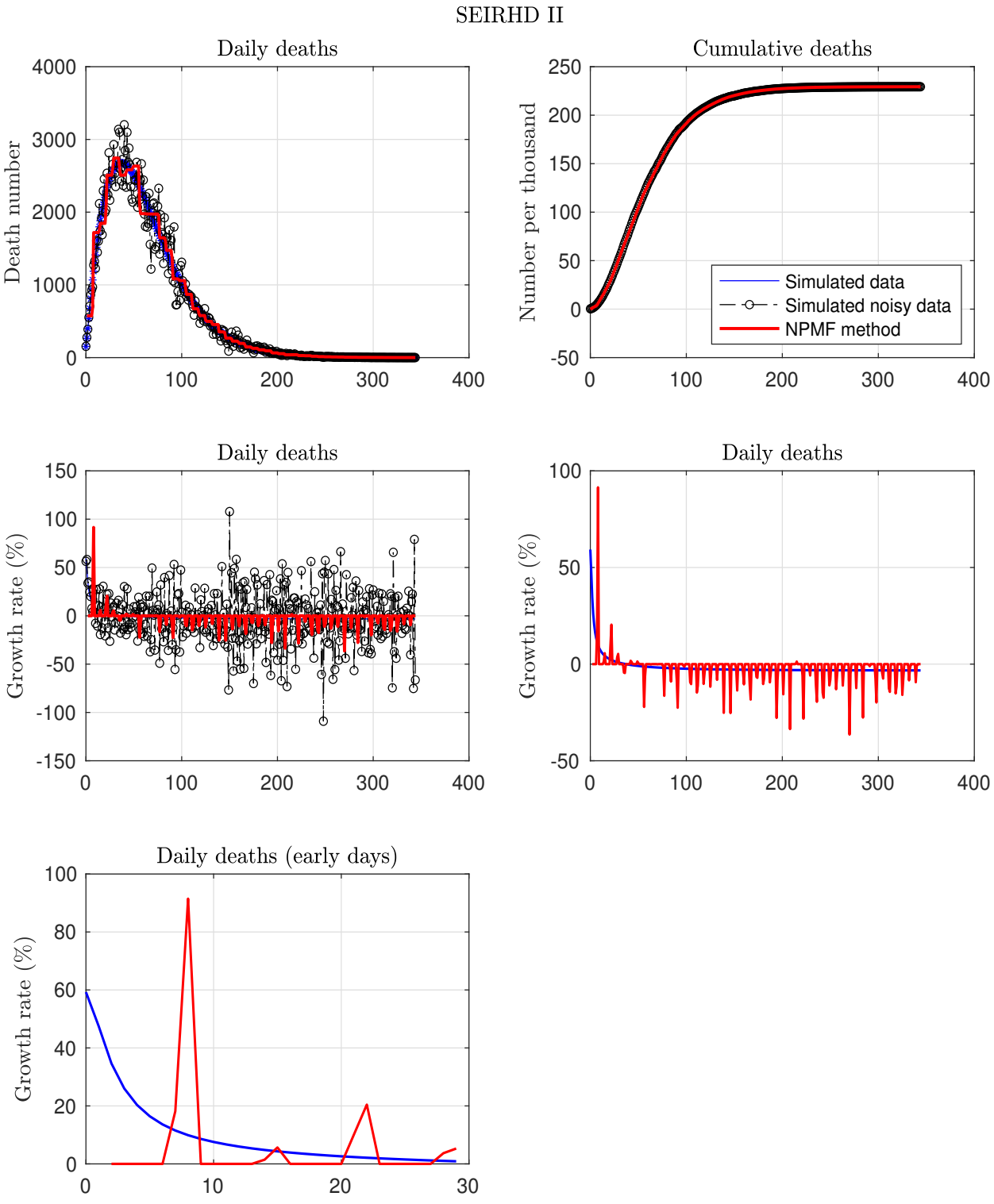


FIGURE 15. Estimation based on the NPMF method applied to artificial death data simulated from theoretical model "SEIRHD II."

TABLE 1. Estimated growth rates (%) of daily deaths across 132 locations worldwide

| Days | Max | 97.5% | 84% | Med | 16% | 2.5% | Min |
|---|---|---|---|---|---|---|---|
| 1 | 139.6 | 88.6 | 32.4 | 7.8 | 2.5 | -3.0 | -20.2 |
| 10 | 43.3 | 23.9 | 13.6 | 4.2 | 0.8 | -3.2 | -15.7 |
| 20 | 20.8 | 10.7 | 6.6 | 2.4 | 0.1 | -5.6 | -24.2 |
| 30 | 15.0 | 7.7 | 4.5 | 1.0 | -1.8 | -6.1 | -22.1 |
| 40 | 16.1 | 6.3 | 3.5 | 0.1 | -3.0 | -6.8 | -19.7 |
| 50 | 13.6 | 5.8 | 2.6 | -0.3 | -3.8 | -7.9 | -17.6 |
| 60 | 14.5 | 7.2 | 2.2 | -0.4 | -3.8 | -7.2 | -15.2 |
| 70 | 14.8 | 7.2 | 1.7 | -0.4 | -3.4 | -5.9 | -7.0 |
| 80 | 20.6 | 5.7 | 1.5 | -0.6 | -3.4 | -5.9 | -7.3 |
| 90 | 42.1 | 7.8 | 2.0 | -0.5 | -3.1 | -5.6 | -8.7 |
| 100 | 28.2 | 5.7 | 2.3 | -0.6 | -3.0 | -5.3 | -14.5 |
| 110 | 18.0 | 5.6 | 2.1 | -0.5 | -3.3 | -5.1 | -19.0 |
| 120 | 5.6 | 4.2 | 1.5 | -0.5 | -3.1 | -4.4 | -16.3 |
| 130 | 37.1 | 3.7 | 1.1 | -0.6 | -2.7 | -4.3 | -12.0 |
| 140 | 24.4 | 6.2 | 1.2 | -0.5 | -2.2 | -4.0 | -8.5 |
| 150 | 17.2 | 6.9 | 1.7 | -0.4 | -1.9 | -3.8 | -6.4 |
| 160 | 63.4 | 10.4 | 2.3 | -0.3 | -1.9 | -3.6 | -8.0 |
| 170 | 25.2 | 9.9 | 3.3 | 0.0 | -1.6 | -3.2 | -11.6 |
| 180 | 18.2 | 9.8 | 4.3 | 0.2 | -1.6 | -3.0 | -12.3 |
| 190 | 33.6 | 9.6 | 5.4 | 0.8 | -1.3 | -3.0 | -12.0 |
| 200 | 15.1 | 9.8 | 5.3 | 0.9 | -1.3 | -2.9 | -11.4 |
| 210 | 12.3 | 7.6 | 4.6 | 1.3 | -1.0 | -3.2 | -10.7 |
| 220 | 59.7 | 7.7 | 4.2 | 1.6 | -1.1 | -2.6 | -9.8 |
| 230 | 11.6 | 6.9 | 3.6 | 1.4 | -0.9 | -2.5 | -8.9 |
| 240 | 28.9 | 7.9 | 3.2 | 1.1 | -1.2 | -2.9 | -8.0 |
| 250 | 6.5 | 6.0 | 2.7 | 0.8 | -1.5 | -3.5 | -7.1 |
| 260 | 10.3 | 6.5 | 2.6 | 0.4 | -1.8 | -4.1 | -14.8 |
| 270 | 8.9 | 6.3 | 2.0 | 0.1 | -2.1 | -4.4 | -8.2 |
| 280 | 8.1 | 4.8 | 1.7 | -0.2 | -2.5 | -3.6 | -5.0 |
| 290 | 9.2 | 5.7 | 1.3 | -0.6 | -2.3 | -3.9 | -4.6 |
| 300 | 9.5 | 4.9 | 1.0 | -0.8 | -2.3 | -3.9 | -4.2 |
| 310 | 2.5 | 1.8 | 0.4 | -0.8 | -2.3 | -3.9 | -4.0 |
| 320 | 0.6 | 0.6 | -0.1 | -0.9 | -1.9 | -4.3 | -4.3 |
| 330 | -0.0 | -0.0 | -0.4 | -1.5 | -3.0 | -5.7 | -5.7 |
| 340 | -1.4 | -1.4 | -1.4 | -1.5 | -1.5 | -1.5 | -1.5 |
| 350 | -1.4 | -1.4 | -1.4 | -1.4 | -1.4 | -1.4 | -1.4 |
| 360 | -1.3 | -1.3 | -1.3 | -1.3 | -1.3 | -1.3 | -1.3 |

*Notes:* The variation of posterior estimates across locations is shown by the maximum (max), 95 percent bounds, 68 percent bounds, median (med), and minimum (min) values.

# 10 Appendix

In this appendix, we report the locations for which we estimate the death trend, provide an algorithm for estimation, and discuss the various SIR models used intrepret our estimation results and to simulate artificial death data for our Monte Carlo study.

## 10.1 Estimation and locations

We estimate the death trend using the daily death data for a total of 132 locations (47 states in the United States, the rest of the United States by grouping the remaining three small states and other U.S. territories, and 86 countries in the rest of the world). For each location, we use the Schwarz criterion (Bayesian information criterion) to select $\mathcal{J}$, the number of MLL density functions.[25] The following lists show the mixture number that is needed for our estimation to fit the distribution of daily deaths in each location:

$\mathcal{J} = 1$ **For the United States:** No location that has a good fit with $\mathcal{J} = 1$.

$\mathcal{J} = 2$ **For the United States:** Texas, New Jersey, Illinois, Michigan, Arizona, Ohio, North Carolina, Connecticut, Maryland, South Carolina, Virginia, Tennessee, Mississippi, Missouri, Alabama, Minnesota, Wisconsin, Colorado, Arkansas, Iowa, Nevada, Kentucky, Oklahoma, Rhode Island, Kansas, New Mexico, West Virginia, Nebraska, South Dakota, Idaho, Utah, North Dakota, Montana, Delaware, New Hampshire, and the rest of the United States.

$\mathcal{J} = 3$ **For the United States:** Arkansas, California, Indiana, Louisiana, Massachusetts, Oregon, Pennsylvania, and Washington.

$\mathcal{J} = 4$ **For the United States:** Florida and Georgia.

$\mathcal{J} = 5$ **For the United States:** New York.

$\mathcal{J} = 1$ **For other countries:** Costa Rica, Ecuador, Georgia, India, Jordan, Libya, and Morocco.

[25] Computing the marginal data density for each of the 132 locations for model selection is prohibitively time consuming.

$\mathcal{J} = 2$ **For other countries:** Austria, Brazil, Mexico, United Kingdom, France, Spain, Peru, Argentina, Colombia, Russia, South Africa, Indonesia, Belgium, Germany, Iraq, Canada, Poland, Ukraine, Netherlands, Pakistan, Sweden, Bangladesh, Saudi Arabia, China, Guatemala, Switzerland, Hungary, Honduras, Dominican Republic, Tunisia, Bulgaria, Moldova, Ireland, Kazakhstan, Bosnia and Herzegovina, Armenia, Afghanistan, Ethiopia, Paraguay, Oman, North Macedonia, Nepal, Nigeria, El Salvador, Denmark, Greece, Croatia, Slovenia, Lebanon, Azerbaijan, Myanmar, Venezuela, and Amazonas.

$\mathcal{J} = 3$ **For other countries:** Albania, Algeria, Australia, Bolivia, Chile, Czechia, Dominican, Egypt, Israel, Italy, Kenya, Latvia, Netherlands, Nevada, Panama, Philippines, Portugal, Romania, Serbia, Sudan, and Zimbabwe.

$\mathcal{J} = 4$ **For other countries:** Lithuania, Slovakia.

$\mathcal{J} = 5$ **For other countries:** Japan, South Korea, and Turkey.

$\mathcal{J} = 6$ **For other countries:** Kyrgyzstan and Iran.

Let $p(\theta_i)$ denote the prior pdf. It follows that the log posterior density function of $\theta_i$ is

$$\begin{aligned}\log p\left(\theta_i \mid \Delta\widetilde{D}_i^{\text{Data}}\right) &= \log \mathcal{L}\left(\Delta\widetilde{D}_i^{\text{Data}} \mid \theta_i\right) + \log p(\theta_i) - \log p\left(\Delta\widetilde{D}_i^{\text{Data}}\right) \\ &\propto \log \mathcal{L}\left(\Delta\widetilde{D}_i^{\text{Data}} \mid \theta_i\right) + \log p(\theta_i)\,,\end{aligned}$$

where $p\left(\Delta\widetilde{D}_i^{\text{Data}}\right)$ is the marginal likelihood, which does not depend on $\theta_i$.

The above estimation procedure is conditional on the value of $d_i$, which does not affect the dynamics of the model's variables except scaling the cumulative deaths $D_i(t)$. We propose the following algorithm to find the scaling parameter $d_i$.

**Algorithm 1.** *Let $d_i^{(0)} > 0$ be the initial value of $d_i$ and $\theta_i^{(0)}$ be the estimate conditional on $d_i^{(0)}$, and denote $\Delta\widehat{D}_{i,t}^{(0)} = f_i\left(t - t_{0,i}, \xi_i^{(0)}\right)$. For $\ell = 1, 2, \cdots$, the algorithm proceeds as follows.*

*(1) Find $d_i$ that minimizes*

$$\log \sum_{t=t_{0,i}}^{T} \left[ D_{i,t}^{Data} - \sum_{s=t_{0,i}}^{t} \Delta\widehat{D}_{i,s}^{(\ell-1)}(1+d_i) D_{i,T}^{Data} \right]^2$$

*and denote this value by* $d_i^{(\ell)} > 0$.

*(2) Estimate* $\theta_i$ *conditional on* $d_i^{(\ell)} > 0$ *as described in this section and denote the estimate by* $\theta_i^{\ell}$.

*(3) Repeat the last two steps until* $d_i^{(\ell)}$ *converges.*

## 10.2 Extensions of the SIR model

In this section we describe the three extensions of the standard SIR model that we consider.

### 10.2.1 SEIRD model

The SEIRD model extends the SIR model by assuming individuals first become exposed to the disease before becoming infected (infectious). At each moment in time, the population $N$ is divided into five states: susceptible $S$, exposed $E$, infected $I$, recovered $R$, and dead $D$. Susceptible individuals are at risk of becoming exposed to the disease. Individuals in the exposed state are not infectious but transition to the infectious state at rate $\sigma$. Note that $1/\sigma$ is the average number of days that an individual has been exposed to the disease but is not yet infectious.

The equations of the model are given by

$$\frac{dS(t)}{dt} = -\mathcal{R}(t)\gamma I(t), \tag{24}$$

$$\frac{dE(t)}{dt} = \mathcal{R}(t)\gamma I(t) - \sigma E(t), \tag{25}$$

$$\frac{dI(t)}{dt} = \sigma E(t) - \gamma I(t), \tag{26}$$

$$\frac{dR(t)}{dt} = (1-\nu)\gamma I(t), \tag{27}$$

$$\frac{dD(t)}{dt} = \nu\gamma I(t). \tag{28}$$

As in the SIR model, the effective reproduction number of the disease is

$$\mathcal{R}(t) \equiv \frac{\beta(t)}{\gamma}\frac{S(t)}{1-D(t)}.$$

We assume that $E(0) = R(0) = D(0) = 0$, $S(0)$ is slightly below $N$ and $I(0)$ is slightly above 0.

The model can be inverted as follows. As before, we have from equations 27 and 28 that

$$\frac{dR(t)}{dt} = \frac{1-\nu}{\nu}\frac{dD(t)}{dt}.$$

Integrating this expression over time and using the initial conditions $D(0) = R(0) = 0$ gives

$$R(t) = \frac{1-\nu}{\nu}D(t).$$

Equation 28 gives

$$I(t) = \frac{1}{\nu\gamma}\frac{dD(t)}{dt},$$

and differentiating this equation we have

$$\frac{dI(t)}{dt} = \frac{1}{\nu\gamma}\frac{d^2D(t)}{dt^2}.$$

Thus, from equation 26, we have

$$E(t) = \frac{1}{\sigma}\left[\frac{1}{\nu}\frac{dD(t)}{dt} + \frac{1}{\nu\gamma}\frac{d^2D(t)}{dt^2}\right].$$

Using the constraint that categories sum to one gives

$$S(t) = 1 - E(t) - I(t) - R(t) - D(t).$$

Note that the model implications for the numbers infected and recovered are the same as the SIR model. The number still susceptible, however, is adjusted to account for the stock of exposed individuals.

Now consider the effective reproduction number. Note that if we sum equations 25 and 26, we get

$$\frac{dE(t)}{dt} + \frac{dI(t)}{dt} = [\mathcal{R}(t) - 1]\,\gamma I(t).$$

Differentiating the equation for $E(t)$ and plugging the other expressions in to the equation above gives

$$\frac{1}{\sigma}\left[\frac{d^2D(t)}{dt^2}+\frac{1}{\gamma}\frac{d^3D(t)}{dt^3}\right]+\frac{1}{\gamma}\frac{d^2D(t)}{dt^2}=\left[\mathcal{R}(t)-1\right]\frac{dD(t)}{dt}.$$

Thus, we get the following expression for the effective reproduction number

$$\mathcal{R}(t)=1+\left(\frac{1}{\gamma}+\frac{1}{\sigma}\right)\frac{\frac{d^2D(t)}{dt}}{\frac{dD(t)}{dt}}+\frac{1}{\sigma\gamma}\frac{\frac{d^3D(t)}{dt^3}}{\frac{dD(t)}{dt}}.$$

Notice that the effective reproduction number is now a function of both the first and second derivatives of daily deaths.

We choose the two parameters $\gamma$ and $\sigma$ so that the model is consistent with typical observed doubling times of daily deaths early on in the pandemic and a basic reproduction number of around 2.5. If we have daily deaths growing exponentially in the early phase of the pandemic with growth rate $\delta$, then

$$\frac{dD(t)}{dt}=\exp(\bar{d}+\delta t).$$

From our formula for the effective reproduction number above

$$\mathcal{R}(0)=1+\left(\frac{1}{\gamma}+\frac{1}{\sigma}\right)\delta+\frac{\delta^2}{\sigma\gamma}.$$

We set $\sigma$ to 0.5 which implies that the average number of days between exposure and infection is 2. The recovery rate $\gamma$ is set at 0.4. At this value, a 30 percent growth rate of daily deaths (doubling time of 2.3 days) corresponds to a basic reproduction number of 2.8.

### 10.2.2 SIHRD model

We now extend the SIR model by adding a state $H$ corresponding to hospitalized. This additional state allows for a longer period from infection to death than in the simpler SIR model. Infected individuals flow from state $I$ to either hospitalized, $H$, or recovered, $R$. Individuals in state $H$ can flow to death, $D$, or recovery, $R$. At each moment in time, the total population $N$ is divided between the five states: $S$, $I$, $H$, $R$, $D$.

The dynamics of the model are given by

$$\frac{dS(t)}{dt}=-\mathcal{R}(t)\gamma I(t), \tag{29}$$

$$\frac{dI(t)}{dt} = [\mathcal{R}(t) - 1]\,\gamma I(t), \tag{30}$$

$$\frac{dH(t)}{dt} = \eta\gamma I(t) - \zeta H(t), \tag{31}$$

$$\frac{dR(t)}{dt} = (1-\nu)\zeta H(t) + (1-\eta)\gamma I(t), \tag{32}$$

$$\frac{dD(t)}{dt} = \nu\zeta H(t), \tag{33}$$

where the definition of the effective reproduction number, $\mathcal{R}(t)$, is the same as in the SIR and SEIRD versions of the model. Note that the parameter $\nu$ is now the fatality rate conditional on hospitalization and $\eta$ is the fraction of the infected population that ends up hospitalized. The parameter $\zeta$ determines the duration of hospital stays. For initial conditions, we assume that $D(0) = R(0) = 0$, $S(0)$ is slightly below $N$, $I(0)$ is slightly above 0, and $H(0)$ may be greater than 0.

We now show how to invert this version of the model to express the effective reproduction number in terms of total deaths and its time derivatives. From equation 33 we have

$$H(t) = \frac{1}{\nu\zeta}\frac{dD(t)}{dt}.$$

Differentiating this equation gives

$$\frac{dH(t)}{dt} = \frac{1}{\nu\zeta}\frac{d^2D(t)}{dt^2}.$$

These results together with equation 31 give

$$I(t) = \frac{1}{\eta\gamma}\left[\frac{1}{\nu}\frac{dD(t)}{dt} + \frac{1}{\nu\zeta}\frac{d^2D(t)}{dt^2}\right].$$

Integrating 32 and the initial conditions imply

$$R(t) = (1-\nu)\zeta\int_{s=0}^{t} H(s)ds + (1-\nu)\zeta H(0) + (1-\eta)\gamma\int_{s=0}^{t} I(s)ds + (1-\eta)\gamma I(0),$$

or

$$R(t) = \frac{1-\nu}{\nu}D(t) + \frac{1-\eta}{\eta}\left[\frac{1}{\nu}D(t) + \frac{1}{\nu\zeta}\frac{dD(t)}{dt}\right] + (1-\nu)\zeta H(0) + (1-\eta)\gamma I(0).$$

where

$$H(0) = \frac{1}{\nu\zeta}\frac{dD(0)}{dt},$$

and

$$I(0) = \frac{1}{\eta\gamma}\left[\frac{1}{\nu}\frac{dD(0)}{dt} + \frac{1}{\nu\zeta}\frac{d^2D(0)}{dt^2}\right].$$

Using the constraint that categories sum to one gives

$$S(t) = 1 - I(t) - H(t) - R(t) - D(t).$$

Having inverted the model, we can now turn to the effective reproduction number. Differentiating our expression for $I(t)$ gives

$$\frac{dI(t)}{dt} = \frac{1}{\eta\gamma}\left[\frac{1}{\nu}\frac{d^2D(t)}{dt^2} + \frac{1}{\nu\zeta}\frac{d^3D(t)}{dt^3}\right],$$

and combining these two expressions with equation 30 yields

$$\frac{1}{\gamma}\left[\frac{d^2D(t)}{dt^2} + \frac{1}{\zeta}\frac{d^3D(t)}{dt^3}\right] = [\mathcal{R}(t) - 1]\left[\frac{dD(t)}{dt} + \frac{1}{\zeta}\frac{d^2D(t)}{dt^2}\right].$$

Thus,

$$\mathcal{R}(t) = 1 + \frac{1}{\gamma}\frac{\left[\frac{d^2D(t)}{dt^2} + \frac{1}{\zeta}\frac{d^3D(t)}{dt^3}\right]}{\left[\frac{dD(t)}{dt} + \frac{1}{\zeta}\frac{d^2D(t)}{dt^2}\right]}.$$

As in the SEIRD model, the reproductive ratio depends on daily deaths and both its first and second derivatives. It also depends on the rate at which individuals transition out of hospitalization, $\zeta$. We set this rate to 1/7 such that the average duration of hospital stays is one week consistent with values reported on the CDC website. We choose $\gamma$ so that our model is consistent with observed doubling times of daily deaths in the early phase of the pandemic when the basic reproduction number in the model is in line with CDC estimates of $\mathcal{R}(0) = 2.5$. If we have daily deaths growing exponentially in the early phase of the

pandemic, then

$$\frac{dD(t)}{dt} = \exp(\bar{d} + \delta t),$$

so

$$\mathcal{R}(0) = 1 + \frac{1}{\gamma}\frac{\left[\delta + \frac{1}{\zeta}\delta^2\right]}{\left[1 + \frac{1}{\zeta}\delta\right]} = 1 + \frac{\delta}{\gamma},$$

which is the same expression as for the simple SIR model. Thus, we set $\gamma = 0.2$, the same value we used for the SIR version. With $\gamma$ set to this value, a 30 percent daily growth rate of new deaths, $\delta = 0.3$, corresponds to a basic reproduction number of 2.5.

### 10.2.3 SEIHRD Model

The SEIHRD model extends the SIR model by adding both the exposed state $E$ and the hospitalized state $H$. In this version of the model the total population $N$ is given by the sum of susceptible individuals in state $S$, exposed in state $E$, infected in $I$, hospitalized in $H$, recovered in $R$, and dead in $D$. The dynamics of the model are given by

$$\frac{dS(t)}{dt} = -\mathcal{R}(t)\gamma I(t), \tag{34}$$

$$\frac{dE(t)}{dt} = \mathcal{R}(t)\gamma I(t) - \sigma E(t), \tag{35}$$

$$\frac{dI(t)}{dt} = \sigma E(t) - \gamma I(t), \tag{36}$$

$$\frac{dH(t)}{dt} = \eta\gamma I(t) - \zeta H(t), \tag{37}$$

$$\frac{dR(t)}{dt} = (1-\nu)\zeta H(t) + (1-\eta)\gamma I(t), \tag{38}$$

$$\frac{dD(t)}{dt} = \nu\zeta H(t), \tag{39}$$

where the effective reproduction number is as defined for the other versions of the model. Initial conditions are $E(0) = R(0) = D(0) = 0$, $S(0)$ slightly below $N$, $I(0)$ slightly above 0, and $H(0) \geq 0$.

We proceed as before with inverting the model. From equation 39 we have

$$H(t) = \frac{1}{\nu\zeta}\frac{dD(t)}{dt}.$$

Differentiating this equation gives

$$\frac{dH(t)}{dt} = \frac{1}{\nu\zeta}\frac{d^2D(t)}{dt^2}.$$

These results together with equation 37 give

$$I(t) = \frac{1}{\eta\gamma}\left[\frac{1}{\nu}\frac{dD(t)}{dt} + \frac{1}{\nu\zeta}\frac{d^2D(t)}{dt^2}\right].$$

Integrating 38 and the initial conditions imply

$$R(t) = (1-\nu)\zeta\int_{s=0}^{t} H(s)ds + (1-\nu)\zeta H(0) + (1-\eta)\gamma\int_{s=0}^{t} I(s)ds + (1-\eta)\gamma I(0),$$

or

$$R(t) = \frac{1-\nu}{\nu}D(t) + \frac{1-\eta}{\eta}\left[\frac{1}{\nu}D(t) + \frac{1}{\nu\zeta}\frac{dD(t)}{dt}\right] + (1-\nu)\zeta H(0) + (1-\eta)\gamma I(0),$$

where

$$H(0) = \frac{1}{\nu\zeta}\frac{dD(0)}{dt},$$

and

$$I(0) = \frac{1}{\eta\gamma}\left[\frac{1}{\nu}\frac{dD(0)}{dt} + \frac{1}{\nu\zeta}\frac{d^2D(0)}{dt^2}\right].$$

Note that differentiating our expression above for $I(t)$ gives

$$\frac{dI(t)}{dt} = \frac{1}{\eta\gamma}\left[\frac{1}{\nu}\frac{d^2D(t)}{dt^2} + \frac{1}{\nu\zeta}\frac{d^3D(t)}{dt^3}\right].$$

Equation 36 implies that

$$E(t) = \frac{1}{\sigma}\left[\frac{dI(t)}{dt} + \gamma I(t)\right],$$

and combining with our expressions for $I(t0$ and $dI(t)/dt$ we have

$$E(t) = \frac{1}{\sigma\eta\nu}\left[\frac{1}{\gamma}\left[\frac{d^2D(t)}{dt^2} + \frac{1}{\zeta}\frac{d^3D(t)}{dt^3}\right] + \left[\frac{dD(t)}{dt} + \frac{1}{\zeta}\frac{d^2D(t)}{dt^2}\right]\right].$$

Finally, we have

$$S(t) = 1 - E(t) - I(t) - H(t) - R(t) - D(t).$$

In terms of measuring the effective reproduction number, this model shares with the SEIRD model that the growth of exposed and infected individuals is determined by

$$\frac{dE(t)}{dt} + \frac{dI(t)}{dt} = [\mathcal{R}(t) - 1]\,\gamma I(t).$$

Differentiating the expression for $E(t)$, plugging it and the expressions for $I(t)$ and $dI(t)/dt$ into the above equation, and rearranging terms gives

$$\mathcal{R}(t) = 1 + \frac{\left(\frac{1}{\sigma} + \frac{1}{\gamma}\right)\frac{d^2D(t)}{dt^2} + \left(\frac{1}{\sigma\gamma} + \frac{1}{\sigma\zeta} + \frac{1}{\gamma\zeta}\right)\frac{d^3D(t)}{dt^3} + \frac{1}{\sigma\gamma\zeta}\frac{d^4D(t)}{dt^4}}{\frac{dD(t)}{dt} + \frac{1}{\zeta}\frac{d^2D(t)}{dt^2}}.$$

Notice that the reproductive ratio now depends not only on the first two derivatives of daily deaths but also the third derivative.

To calibrate the parameters $\gamma$, $\sigma$, and $\zeta$ we proceed as before. The parameter $\zeta$ is set to 1/7 so that the average duration of a hospital stays is 7 days in line with CDC reports. The parameters $\gamma$ and $\sigma$ are set to 0.4 and 0.5. These are the same values used in the SEIRD version of the model. This combination of parameter values implies that a 30 percent growth rate of new daily deaths corresponds with a basic reproduction number, $\mathcal{R}(0)$, of 2.8.

Artificial death data for the Monte Carlo exercise presented in Section V is generated by simulating the SEIRHD model assuming a path for the normalized transmission rate which has it falling rapidly early on in the pandemic from an initial level above one to one and remaining there. For SEIRHD I, $\beta$ is set such that the initial level of the normalized transmission rate, $\beta/\gamma = 1.75$. This assumption leads to a relatively low initial growth rate of daily deaths of 12 percent as shown the bottom right panel of Figure 5. In the case of SEIRHD II, $\beta$ is set to a higher value such that the initial level of the normalized transmission rate $\beta/\gamma = 6$. This parameterization yields a much higher initial growth rate of daily deaths,

49 percent, as shown in the bottom right panel of Figure 6. In both simulations, time is normalized such that $t = 0$ corresponds to the date when cumulative deaths reach 25. The normalized transmission rate is assumed to remain constant at its initial level during the first 30 days ($t \leq 30$) before dropping to one.

## References

Anderson, R. M., H. Heersterbeek, D. Klinkenberg and T. D. Hollingsworth, "How will country-based mitigation measures influence the course of the COVID-19 epidemic?," *The Lancet* (March 2020).

Aspelund, K. M., M. C. Droste, J. H. Stock and C. D. Walker, "Identification and Estimation of Undetected COVID-19 Cases Using Testing Data from Iceland," Working Paper 27528, National Bureau of Economic Research, July 2020.

Atkeson, A., "On Using SIR Models to Model Disease Scenarios for COVID-19," *Federal Reserve Bank of Minneapolis Quarterly Review* (June 2020).

Atkeson, A., K. Kopecky and T. Zha, "Estimating and Forecasting Disease Scenarios for COVID-19 with an SIR Model," Working Paper 27335, National Bureau of Economic Research, June 2020a.

———, "Four Stylized Facts About COVID-19," Working Paper 27719, NBER, August 2020b.

———, "Behavior and the Transmission of COVID-19," *American Economic Association Papers and Proceedings* 111 (May 2021), 356–360.

———, "Estimation Results for All Locations: Supplemental Appendix to 'Four Stylized Facts About COVID-19'," Unpublished manuscript, UCLA and Federal Reserve Bank of Atlanta, 2023.

Baqaee, D., E. Farhi, M. Mina and J. H. Stock, "Policies for a Second Wave," *Brookings Papers on Economic Activity* (July Forthcoming).

Bodenstein, M., G. Corsetti and L. Guerrieri, "Social Distancing and Supply Disruptions in a Pandemic," *Quantitative Economics* (Forthcoming).

Bootsma, M. C. J. and N. M. Ferguson, "The Effect of Public Health Measures on the 1918 Influenza Pandemic in U.S. Cities," *Proceedings of the National Academy of Sciences* 104 (May 2007), 7588–7593.

Bornkamp, B. and K. Ickstadt, "Bayesian Nonparametric Estimation of Continuous Monotone Functions with Applications to Dose-Response Analysis," *Biometrics* 65 (March

2009), 198–205.

Chowell, G., L. Sattenspiel, S. Bansal and C. Viboud, "Mathematical models to characterize early epidemic growth: A Review," *Physical Life Review* 18 (September 2016), 66–97.

Correia, S., S. Luck and E. Verner, "Pandemics Depress the Economy, Public Health Interventions Do Not: Evidence from the 1918 Flu,," *Journal of Economic History* 82 (December 2022), 917–957.

Droste, M. and J. H. Stock, "Adapting to the COVID-19 Pandemic," *American Economic Association Papers and Proceedings* 111 (May 2021), 351–355.

Eichenbaum, M. S., S. Rebelo and M. Trabandt, "The Macroeconomics of Epidemics," Working Paper 26882, National Bureau of Economic Research, March 2020.

Eksin, C., K. Paarporn and J. S. Weitz, "Systematic biases in disease forecasting – The role of behavior change," *Epidemics* 27 (June 2019), 96–105.

Farboodi, M., G. Jarosch and R. Shimer, "Internal and External Effects of Social Distancing in a Pandemic," Working Paper 27059, National Bureau of Economic Research, April 2020.

Ferguson, N. M., "Capturing Human Behavior," *Nature* 446 (April 2007), 733.

Ferguson, N. M., D. A. T. Cummings, C. Fraser, J. C. Cajka, P. C. Cooley and D. S. Burke, "Strategies for Mitigating an Influenza Pandemic," *Nature* 442 (July 2006), 448–452.

Fernandez-Villaverde, J. and C. I. Jones, "Estimating and Simulating a SIRD Model of COVID-19 for Many Countries, States, and Cities," Working Paper 27128, NBER, April 2020.

Flaxman, S., S. Mishra, A. Gandy, H. J. T. Unwin, T. A. Mellan, H. Coupland, C. Whittaker, H. Zhu, T. Berah, J. W. Eaton, M. Monod, P. N. Perez-Guzman, N. Schmit, L. Cilloni, K. E. C. Ainslie, M. Baguelin, A. Boonyasiri, O. Boyd, L. Cattarino, L. V. Cooper, Z. Cucunubá, G. Cuomo-Dannenburg, A. Dighe, B. Djaafara, I. Dorigatti, S. L. van Elsland, R. G. FitzJohn,

K. A. M. Gaythorpe, L. Geidelberg, N. C. Grassly, W. D. Green, T. Hallett, A. Hamlet, W. Hinsley, B. Jeffrey, E. Knock, D. J. Laydon, G. Nedjati-Gilani, P. Nouvellet, K. V. Parag, I. Siveroni, H. A. Thompson, R. Verity, E. Volz, C. E. Walters, H. Wang, Y. Wang, O. J. Watson, P. Winskill, X. Xi, P. G. Walker, A. C. Ghani, C. A. Donnelly, S. M. Riley, M. A. C. Vollmer, N. M. Ferguson, L. C. Okell, S. Bhatt and I. C. C.-. R. Team, "Estimating the effects of non-pharmaceutical interventions on COVID-19 in Europe," *Nature* (2020).

Funk, S., S. Bansal, C. T. Bauch, K. T. Eames, W. J. Edmunds, A. P. Galvanie and P. Klepac, "Nine challenges in incorporating the dynamics of behaviour in infectious diseases models," *Epidemics* 10 (2015), 21–25.

Gans, J. S., "The Economic Consequences of R = 1: Towards a Workable Behavioural Epidemiological Model of Pandemics," Working Paper 27632, National Bureau of Economic Research, July 2020.

Germann, T. C., K. Kadau, I. M. J. Longini and C. Macken, "Mitigation Strategies for Pandemic Influenza in the United States," *Proceedings of the National Academy of Sciences* 103 (April 2006), 5935–5940.

Guerrieri, V., G. Lorenzoni, L. Straub and I. Werning, "Macroeconomic Implications of COVID-19: Can Negative Supply Shocks Cause Demand Shortages?," Working Paper 26918, National Bureau of Economic Research, April 2020.

Halloran, E. M., N. M. Ferguson, S. Eubank, I. M. J. Longini, D. A. T. Cummings, B. Lewis, S. Xu, C. Fraser, A. Vullikanti, T. C. Germann, D. Wagener, R. Beckman, K. Kadau, C. Barrett, C. A. Macken, D. S. Burke and P. C. Cooley, "Modeling Targeted Layered Containment of an Influenza Pandemic in the United States," *Proceedings of the National Academy of Sciences* 105 (March 2008), 4639–4644.

Hamilton, J. D., "A New Approach to the Economic Analysis of Nonstationary Time Series and the Business Cycle," *Econometrica* 57 (1989), 357–384.

Hay, S. I., "COVID-19 scenarios for the United States," *medRxiv* (2020).

Hollingsworth, T. D., D. Klinkenberg, H. Heersterbeek and R. M. Anderson, "Mitigation Strategies for Pandemic Influenza A: Balancing Conflicting Policy Objectives," *PLOS Computational Biology* 7 (February 2011), 1–11.

Kaplan, G., B. Moll and G. Violante, "Pandemics According to HANK," Unpublished Manuscript, May 2020.

Keppo, J., E. Quercioli, M. Kudlyak, L. Smith and A. Wilson, "The Behavioral SI* Model, with Applications to the Swine Flu and COVID-19 Pandemics," Unpublished Manuscript, April 2021.

Kissler, S. M., C. Tedijanto, E. Goldstein, Y. H. Grad and M. Lipsitch, "Projecting the transmission dynamics of SARS-COV-2 through the postpandemic period," *Science* 10.1126/science.abb5793 (April 2020).

Korevaar, H. M., A. D. Becker, I. F. Miller, B. T. Grenfell, C. J. E. Metcalf and M. J. Mina, "Quantifying the impact of US state non-pharmaceutical interventions on COVID-19 transmission," *medRxiv* (2020).

Liu, Z., P. Wang and T. Zha, "Land-Price Dynamics and Macroeconomic Fluctuations," *Econometrica* 81 (May 2013), 1147–1184.

Madsen, H., *Time Series Analysis* (Chapman and Hall/CRC, 2007).

Moore, K. A., M. Lipsitch, J. M. Barry and M. T. Osterholm, "The Future of the COVID-19 Pandemic: Lessons Learned from Pandemic Influenza," Viewpoint Part 1, CIDRAP, the University of Minnesota, April 2020.

Murray, C. J., "Forecasting the impact of the first wave of the COVID-19 pandemic on hospital demand and deaths for the USA and European Economic Area countries," *medRxiv* (2020).

Phillipson, T. and R. A. Posner, *Private Choices and Public Health: the AIDS Epidemic in an Economic Perspective* (Harvard University Press, 1993).

Shively, T. S., T. W. Sager and S. G. Walker, "A Bayesian Approach to Non-Parametric Monotone Function Estimation," *Journal of the Royal Statistical Society. Series B (Statistical Methodology)* 71 (January 2009), 159–175.

Toxvaerd, F., "Equilibrium Social Distancing," Working Paper 2020/8, Cambridge-INET, March 2020.

Waggoner, D. F., H. Wu and T. Zha, "Dynamic Striated Metropolis-Hastings Sampler for High-Dimensional Models," *Journal of Econometrics* 192 (2016), 406–420.